The Astrophysical Journal, 1004:104 (18pp), 2026 June 10 https://doi.org/10.3847/1538-4357/ae680a

XRISM/Resolve Observations of Hercules X-1: Vertical Structure and Kinematics of the Disk Wind

Peter Kosec[1], Laura Brenneman[1], Erin Kara[2], Teruaki Enoto[3], Takuto Narita[3], Koh Sakamoto[3], Rüdiger Staubert[4], Francesco Barra[5], Andrew Fabian[6], Jon M. Miller[7], Ciro Pinto[8], Daniele Rogantini[9], Dominic Walton[10], and Yutaro Nagai[3]
[1] Center for Astrophysics—Harvard & Smithsonian, Cambridge, MA, USA; peter.kosec@cfa.harvard.edu
[2] MIT Kavli Institute for Astrophysics and Space Research, Massachusetts Institute of Technology, Cambridge, MA 02139, USA
[3] Department of Physics, Graduate School of Science, Kyoto University, Kitashirakawa Oiwake-cho, Sakyo-ku, Kyoto 606-8502, Japan
[4] Institut für Astronomie und Astrophysik, Universität Tübingen, Sand 1, D-72076 Tübingen, Germany
[5] Università degli Studi di Palermo, Dipartimento di Fisica e Chimica, via Archirafi 36, I-90123 Palermo, Italy
[6] Institute of Astronomy, Madingley Road, Cambridge, CB3 0HA, UK
[7] Department of Astronomy, University of Michigan, Ann Arbor, MI 48109, USA
[8] INAF—IASF Palermo, Via U. La Malfa 153, I-90146 Palermo, Italy
[9] Department of Astronomy and Astrophysics, The University of Chicago, Chicago, IL 60637, USA
[10] Centre for Astrophysics Research, University of Hertfordshire, UK
Received 2025 December 9; revised 2026 April 10; accepted 2026 April 30; published 2026 June 8

Abstract

X-ray binary accretion disk winds can carry away a significant fraction of the matter transferred from the companion and hence strongly affect the accretion flow and the long-term evolution of the binary. However, accurate mass outflow rate measurements are challenging due to uncertainties in our understanding of the 3D wind structure. Most studies employ absorption line spectroscopy, which only gives us a single sightline through the wind streamlines. Hercules X-1 is a peculiar X-ray binary which allows us to avoid this issue, as its warped, precessing accretion disk naturally presents a range of sightlines through the vertical structure of its disk wind. Here we present the first results from a large, coordinated campaign on Her X-1 led by the new XRISM observatory (with an exposure of 210 ks) and supported by XMM-Newton, NuSTAR, and Chandra. We perform a time-resolved analysis and constrain the wind properties. With XRISM/Resolve, we directly detect the Her X-1 orbital motion with an amplitude of 170 km s^{-1} in the evolution of the wind velocity. After correcting for this effect, we observe an increase in wind velocity from 250 to 600 km s^{-1} as the wind rises to greater heights above the disk. The wind column density decreases with increasing height, as expected, but its ionization parameter $\log(\xi/\mathrm{erg\ cm\ s^{-1}})$ evolves only weakly from 3.65 to 3.9 as the wind expands away. Additionally, we detect a new orbital dependence of the wind properties, revealing a likely second component that appears only briefly after the eclipse by the secondary star.

Unified Astronomy Thesaurus concepts: Accretion (14); High energy astrophysics (739); Neutron stars (1108)

1. Introduction

Blueshifted absorption lines imprinted by accretion disk winds are some of the most distinct spectral features of X-ray binaries. First discovered using the ASCA observatory (Y. Ueda et al. 1998; T. Kotani et al. 2000), our understanding of disk winds and their observational signatures has significantly improved over the last ∼2 decades thanks to Chandra and XMM-Newton (e.g., Y. Ueda et al. 2004; M. Díaz Trigo et al. 2012). More recently, signatures of disk winds in X-ray binaries were also discovered in the UV, optical, and infrared energy bands (T. Muñoz-Darias et al. 2019; J. Sánchez-Sierras & T. Muñoz-Darias 2020; N. Castro Segura et al. 2022).

Typically, disk winds in X-ray binaries reach velocities up to 1000 km s^{-1} (for a review, see J. Neilsen & N. Degenaar 2023), much lower than certain types of wide-angle outflows observed in accreting supermassive black holes (e.g., F. Tombesi et al. 2010) and ultraluminous X-ray sources (e.g., C. Pinto et al. 2016; P. Kosec et al. 2018) that can exhibit velocities in excess of 10% of the speed of light. Nevertheless, the X-ray binary disk wind mass outflow rates can be of the same order as the mass accretion rates onto the compact object (J. C. Lee et al. 2002; P. Kosec et al. 2020). Therefore, by transporting this significant mass as well as angular momentum outside the binary system, they can affect the long-term evolution of X-ray binaries (B. E. Tetarenko et al. 2018; M. Gallegos-Garcia et al. 2024).

Despite being known for over 2 decades, much is still unknown about these phenomena in X-ray binaries, including their exact physical launching mechanism. It is also challenging to accurately quantify their mass outflow rates and thus constrain the actual impact on their binary systems and neighborhoods. One of the reasons why this is difficult is because disk winds are mainly studied through their X-ray absorption lines, and thus are only sampled along a single line of sight toward the compact X-ray source. X-ray absorption line spectroscopy is the most straightforward way to understand the wind properties such as its column density, ionization parameter, and velocity, but it gives us a limited view of the complex 3D structure of the outflow. Statistical studies of samples of X-ray binaries (G. Ponti et al. 2012; M. Parra et al. 2024) suggest that the vertical wind structure is not spherical but equatorial (with a ∼10° half-opening angle), but this

parameter cannot typically be constrained in any individual source.

Hercules X-1 (hereafter Her X-1) is an X-ray pulsar, an X-ray binary powered by a highly magnetized neutron star rotating every 1.2 s (H. Tananbaum et al. 1972). It is famous for its 35 day cycle of high and low flux states, introduced by a warped, precessing accretion disk that is seen almost edge-on (J. I. Katz 1973; D. Gerend & P. E. Boynton 1976). This warped disk precession changes our line of sight through the accretion flow, and at certain times of the 35 day precession cycle, outer parts of the disk obscure our view of the inner accretion flow (which produces most of the X-rays). At other times, the inner accretion flow is uncovered, resulting in two high-flux periods during each 35 day cycle named the Main High and the Short High states.

The disk precession offers a unique and powerful tool to study the 3D properties of the disk wind of Her X-1, as our time-variable sightline intersects the wind streamlines at different locations over the 35 day precession cycle, specifically at different heights above the accretion disk. A schematic showing this situation is shown in Figure 1 of P. Kosec et al. (2023a). According to the model of the Her X-1 warped disk precession by D. M. Scott et al. (2000), the inner and outer rings of the accretion disk precess by 11° and 20°, respectively, over the 35 day precession cycle (this motion is shown from the point of view of the neutron star in Figure 2 of their paper). A significant part of the wind structure then crosses our line of sight during the 35 day cycle, assuming that the structure is equatorial with a relatively small opening angle (as observed in other X-ray binaries, G. Ponti et al. 2012).

Thus, we can explore the wind vertical structure through its X-ray absorption lines by sampling the wind properties over a range of precession phases. We previously studied Her X-1 with XMM-Newton and Chandra and showed that the disk wind is present in X-ray absorption during both the Main and Short High states (P. Kosec et al. 2020, 2023b) and has a velocity of $250-1000\,\mathrm{km\,s^{-1}}$ and an ionization parameter of $\log(\xi/\mathrm{erg\,cm\,s^{-1}})$ of 3−4, consistent with typical X-ray binary disk winds. P. Kosec et al. (2020) and P. Kosec et al. (2023a) performed a detailed study of the wind during the Main High state and leveraged the disk precession to produce a 2D map of this outflow, and estimated the mass outflow rate to be as high as 70% of the mass transfer rate from the secondary star.

Typical accretion disk winds detected in X-ray binaries are highly ionized, with ionization parameters around $\log(\xi/\mathrm{erg\,cm\,s^{-1}})$ of 4. Some of their strongest observational signatures are therefore in the Fe K energy band, with particularly strong transitions of Fe XXV (at 6.7 keV) and Fe XXVI (at 6.96 keV). The recently launched XRISM observatory (M. S. Tashiro 2022) offers a generational leap in our spectral capability in this energy band. The microcalorimeter Resolve instrument onboard XRISM achieves a spectral resolution of 4.5 eV at 6 keV (Y. Ishisaki et al. 2022), which is roughly ∼10× the spectral resolution of Chandra HETG gratings (first order) and ∼30× the spectral resolution of typical X-ray CCDs such as EPIC onboard XMM-Newton at these energies. Therefore, XRISM is an outstanding instrument to study the physics of accretion disk winds in X-ray binaries, providing a precision and detail much greater than has previously been possible.

In 2024 September, we carried out a large observational campaign on Her X-1 led by XRISM. The aim of the campaign is to study and understand the 3D structure of the Her X-1 disk wind with unprecedented precision (P. Kosec et al. 2024). To achieve this goal, we observed a significant fraction of a single Main High state of Her X-1 for a duration of ∼400 ks (resulting in a ∼200 ks clean exposure time after accounting for XRISM's low-earth orbit). In addition to this XRISM observation, we also obtained simultaneous observations with Chandra (50 ks), XMM-Newton (80 ks), and NuSTAR (40 ks), each covering part of the long XRISM exposure.

This is the first manuscript describing the 2024 XRISM observations of Her X-1. Here we focus on the evolution of the wind properties with the Her X-1 precession phase. Thanks to the excellent spectral capabilities of XRISM, we are for the first time able to track the kinematics of the wind and their variations with the precession phase. The manuscript is structured as follows. In Section 2, we describe the 2024 September observational campaign on Her X-1 and the preparation and reduction procedures for all datasets. In Section 3, we present the results of this study using phenomenological as well as physically motivated spectral fitting approaches. In Section 4, we discuss the results and in Section 5 we summarize the conclusions of this paper. Throughout the paper, we assume a distance of 6.1 kpc for Her X-1 (D. A. Leahy & M. H. Abdallah 2014).

2. Observations and Data Preparation

2.1. 2024 Observations of Hercules X-1

The XRISM Her X-1 observation began on 2024 September 10 with a gross duration of 380 ks, resulting in a clean exposure of 210 ks. A raw XRISM lightcurve of the observation is shown in Figure 1. The aim of the campaign was to begin observing as close as possible to the Turn-on of the Main High state, when our line of sight samples the disk wind at low heights above the disk (just after the disk itself uncovered our line of sight toward the X-ray source), and continue observing for a significant fraction of the High state as our sightline rises to greater heights above the disk. Thanks to an accurate Turn-on ephemeris prediction using the method of R. Staubert et al. (2016), we were able to observe the transition from the Low into the Main High state roughly 30 ks after the beginning of the XRISM exposure. By using XRISM and Chandra lightcurves and finding the time when Her X-1 reached ∼50% of the typical X-ray flux during the high-flux state for the first time, we determined that the Turn-on occurred at MJD = 60563.457. We define the Her X-1 precession phase at time t as $T_0 + t/P$, where T_0 is the Turn-on time and P is the precession cycle duration. The long-term average is 34.85 days; however, for this specific cycle, the duration between the two consecutive Main High Turn-on moments was 34.04 days (R. Staubert et al. 2026, in preparation).

With XRISM we observed 3 nearly complete High state binary orbital periods (the orbital period is roughly 1.7 days, H. Tananbaum et al. 1972). Hereafter, these orbits are denoted Orbit 1, Orbit 2, and Orbit 3, respectively. In addition to the high flux intervals, we also observed several periods of absorption dips and two complete and one partial eclipses. We note that this paper only focuses on high flux intervals, and all eclipse, Low state, and absorption dip state data were excluded.

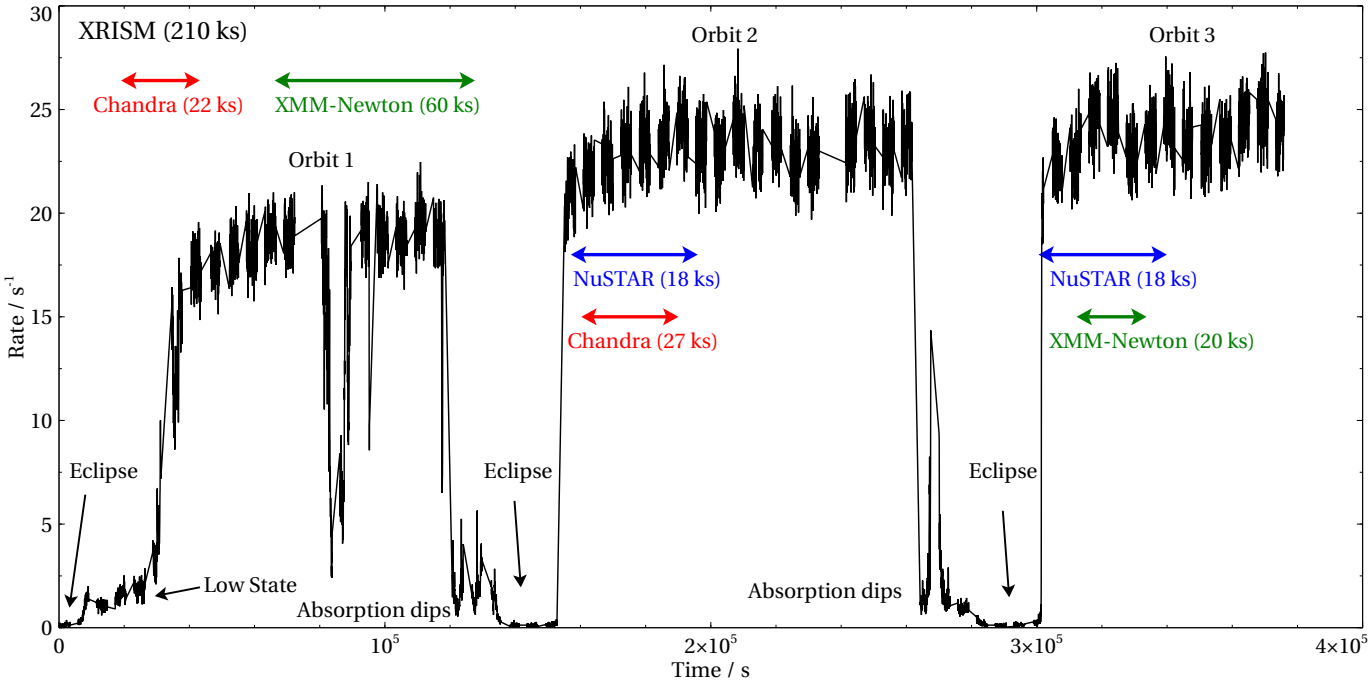

Figure 1. Raw XRISM lightcurve (events of all qualities included) from the 2024 September campaign on Her X-1. Time $T = 0$ corresponds to the beginning of the XRISM observation at MJD = 60563.09653. Horizontal arrows show the overlaps of simultaneous observations with XMM-Newton, Chandra, and NuSTAR as well as their durations. The approximate clean exposures are given in the legend for each observatory. Some of the notable events are described, including our numbering scheme of individual Her X-1 orbits.

As the XRISM gate valve was closed, we also requested Director's Discretionary Time from XMM-Newton (F. Jansen et al. 2001) to capture the soft X-rays of Her X-1, primarily using the reflection grating spectrometers (RGS). XMM-Newton performed one observation which overlapped with Orbit 1, and one observation during Orbit 3 (80 ks total exposure time). We further triggered our Guaranteed Time Observations with Chandra (M. C. Weisskopf et al. 2000) and performed two simultaneous observations with the Chandra HETG gratings during Orbits 1 and 2, with a total exposure of 50 ks. Finally, to capture the hard X-rays above 17 keV, we triggered our Guest Observer program with NuSTAR (F. A. Harrison et al. 2013) and observed Her X-1 for ∼40 ks in two snapshots during Orbits 2 and 3. The approximate timings of all simultaneous observations are shown alongside the XRISM lightcurve in Figure 1.

Further details of all observations taken during the 2024 campaign on Her X-1 are listed in Table 3 in Appendix A.

2.2. XRISM Data Reduction

We reduced all XRISM data using HEASOFT V6.35.1 with the CALDB version 20250315. We followed standard data reduction routines described in the XRISM ABC Data Reduction Guide.[11] We extracted events from the full Resolve array except the calibration pixel (12) and pixel 27, which is known to show abnormal gain behavior. We only used high- and medium-quality primary events (Hp and Mp events), which were extracted into separate spectral files and fitted simultaneously without stacking. Typically, Mp event count rates were 10%−20% of the Hp count rates during Her X-1 high flux periods analyzed in this paper. We generated the response matrix files and ancillary response files using RSLMKRMF and XAARFGEN, respectively, and used XL-sized XRISM response files for all spectral analysis. The data were binned according to the optimal binning scheme (J. S. Kaastra & J. A. M. Bleeker 2016) using the FTOOL routine FTGRPPHA. Finally, the data were converted from OGIP format into SPEX format using the TRAFO routine. Since Her X-1 is a very bright source during its high flux periods, we did not use any generated XRISM background spectra. As the gate valve was closed during the Her X-1 observation, no source counts are registered below 1.8 keV. We therefore used the Resolve data between 1.8 and 12 keV. Data in the range between 12 and 17.5 keV were excluded as no atomic features are expected in this energy range and the higher statistics NuSTAR spectra are available. The XRISM data were separated into multiple intervals in order to perform a time-resolved wind study. Further details of the time-resolved XRISM data slices are listed in Appendix A. We did not use any data from the Xtend instrument in this study, as its spectral resolution is not sufficient for a detailed disk wind analysis performed here.

2.3. XMM-Newton Data Reduction

XMM-Newton data were reduced using the XMM-Newton Scientific Analysis System (SAS) package version 21.0.0. We processed the raw RGS (J. W. den Herder et al. 2001) data with RGSPROC using default source and background extraction regions. Considering the brightness of Her X-1, we did not exclude any periods of high background. The default background regions were strongly contaminated by source counts and hence we used blank field background spectra instead, following the same approach as P. Kosec et al. (2023a). The final RGS spectral files were converted into SPEX format using the TRAFO routine, and binned by a factor of 3 directly within SPEX to achieve oversampling of the instrumental resolution by roughly a factor of 3. RGS 1 and 2 data were always fitted

[11] https://heasarc.gsfc.nasa.gov/docs/xrism/analysis/

simultaneously without any stacking. For spectral fitting, we used the 7.2 Å (1.7 keV) to 36 Å (0.35 keV) wavelength range.

We also used data from the European Photon Imaging Camera (EPIC-pn; L. Strüder et al. 2001). The EPIC-pn camera was operated in Timing mode and the data were processed with the EPPROC routine and extracted using EVSELECT. Only events of PATTERN $\leqslant 4$ (single and double) were accepted as valid events. No periods of background flaring had to be excluded for these observations. The source region was a rectangle centered on Her X-1 (RAWX coordinates between 15 and 56), and the background region was a narrow rectangle as far away on the chip from the source as possible (RAWX coordinates between 2 and 5). To mitigate pile-up, we also excluded a single central pixel column for observation 0953011401 and the central two pixel columns for observation 0953011501. The data were grouped using SPECGROUP to oversample the spectral resolution of EPIC-pn by a factor of at most 3 and also to achieve Gaussian statistics, and finally converted into SPEX format using TRAFO. They were used in the energy range from 2 to 10 keV only for a comparison with the XRISM Resolve data and not for wind parameter estimates.

2.4. NuSTAR Data Reduction

The NuSTAR data were reduced using standard procedures with the NuSTAR Data Analysis Software. The data were first processed using the NUPIPELINE routine, and the spectral files were extracted using the NUPRODUCTS routine. The source regions were circles centered on Her X-1 with a radius of 90″, and the background regions were larger circles away from the source with a radius of 140″. FPMA and FPMB data were extracted separately and fitted simultaneously without stacking. The spectra were binned with FTGRPPHA according to the optimal binning scheme and used in the energy range between 10 and 75 keV. The data below 10 keV were not needed as higher-resolution XRISM Resolve spectra were available. The 10−12 keV region was used for cross calibration between XRISM and NuSTAR.

3. Results

All data were fitted in the SPEX fitting package (J. S. Kaastra et al. 1996) version 3.07.03 by minimizing the Cash statistic (C-stat, W. Cash 1979). All uncertainties are provided at 1σ significance.

Thanks to the excellent spectral resolution of XRISM/Resolve, we are able for the first time to separate the various spectral features in the complex Fe K band of Her X-1. With previous XMM-Newton and Chandra spectra, we were able to determine the presence of the strongest emission lines (P. Kosec et al. 2022) and the disk wind absorption (P. Kosec et al. 2023a) in this band, but much uncertainty remained due to crowding of spectral features at these energies. The time-averaged high-flux XRISM/Resolve spectrum (from all three orbits combined), alongside a simultaneous XMM-Newton EPIC-pn spectrum, is shown in Figure 2.

XRISM clearly resolves several spectral components in the Fe K band. A narrow Fe I Kα line is strongly detected and the Kα1 and Kα2 components are partially resolved. Blueshifted absorption from the accretion disk wind is also present. The strongest feature is the absorption line of Fe XXVI (Lyα1 and Lyα2 components are observed), but Fe XXV absorption is also present, although much weaker than Fe XXVI. The ratio of these two transitions indicates a high ionization degree of the wind. For the first time, we also detect a narrow Fe I Kβ emission line. Finally, all of this narrow spectral structure is superimposed on a highly broadened Fe K complex known from previous Her X-1 studies (P. Kosec et al. 2022).

All narrow components are broadened beyond the instrumental resolution of XRISM. This is expected considering the orbital motion of Her X-1 with a projected orbital velocity of 170 km s^{-1} (J. E. Deeter et al. 1981), which smooths all orbital-averaged spectra by this velocity width. Additionally, the narrow Fe I Kα line is consistent with having at least two kinematic components: a very narrow one (with a width of $\sim$100 km s^{-1}) and a slightly broadened one (with a width of $\sim$1000 km s^{-1}).

Thanks to the very long exposure with XRISM, we are able to probe how the wind varies with time (and Her X-1 precession phase). To show this visually, we extracted data from the three Her X-1 orbits into separate spectra and focused specifically on the Fe XXVI absorption line energy region. This is shown in Figure 3. The Fe XXVI doublet clearly varies from orbit to orbit. Its strength decreases over time from Orbit 1 to 2 to 3, as the 35 day cycle precession phase increases, in agreement with previous Her X-1 observations (P. Kosec et al. 2023a). For the first time, thanks to XRISM, we are also able to see shifts in its centroid energy and width over time. The line appears to broaden with time and consistently shifts to higher energies. Therefore, the optical depth of the outflow in Fe XXVI decreases, and its projected velocity increases, as well as its velocity width. A similar evolution is also observed for Fe XXV, but at a lower signal-to-noise ratio.

In the following sections we perform a more detailed time-resolved, quantitative analysis of these variations. The XRISM exposure is split into a number of intervals to understand how the relevant absorber parameters evolve with the phases of the orbital ($\sim$1.7 days) and superorbital ($\sim$35 days) cycles seen in Her X-1. The interval sizes were defined adaptively to maximize the signal-to-noise ratio within each interval, while preserving as much time resolution as possible, and are different for the different analyses performed below. The signal-to-noise ratio depends on the combination of the X-ray flux seen from Her X-1 during the interval, both the optical depth and the width of the absorption lines, and the exact spectral model used to describe the absorber. We explored a range of interval sizes for each analysis, starting from small intervals and increasing their exposure until the best-fitting wind parameter uncertainties were small enough to track the systematic variation in the wind properties.

In Section 3.1 we describe the setup of the spectral fitting model. In Section 3.2 we model the wind absorption features with a phenomenological spectral model which allows us to assess the absorption lines in the most model-independent manner. Finally, in Section 3.3 we apply a photoionization model to determine the physical parameters of the disk wind.

3.1. Spectral Model Setup

We use a phenomenological spectral model to describe the continuum and line emission from Her X-1 before modeling the disk wind absorption. Each time interval of the time-resolved analysis is fitted independently. We fit the XRISM Hp and Mp data in two separate spectra using a cross-calibration constant. Its value is in all cases within 1% of unity. The XRISM data are fitted simultaneously with NuSTAR data to

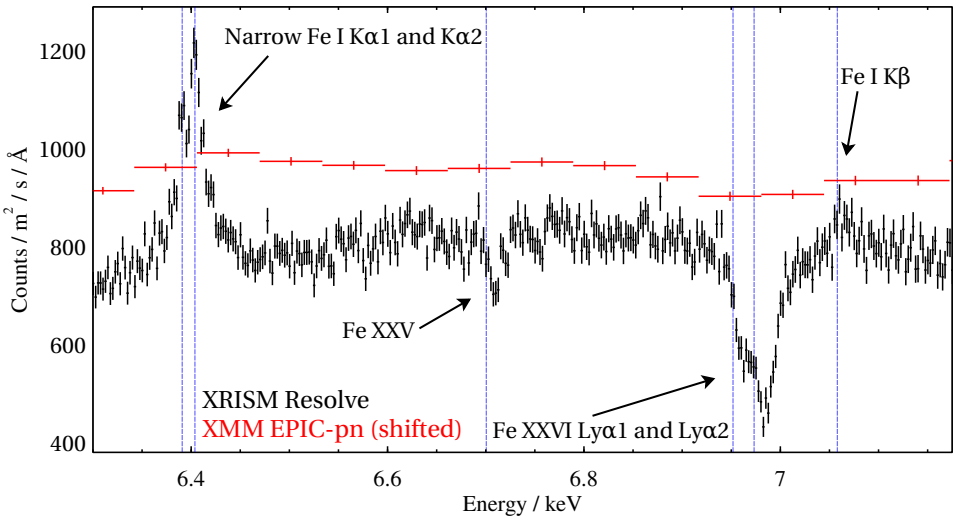

Figure 2. Comparison between the time-averaged high-flux XRISM/Resolve spectrum, focusing on the Fe K energy band, with simultaneous data from XMM-Newton EPIC-pn. The most notable spectral features are described and their rest-frame energies are shown with blue vertical dashed lines. The EPIC-pn data were shifted in energy to account for the known gain shift issue at high count rates (see Appendix A of P. Kosec et al. 2022) and also in flux by a constant for visual purposes.

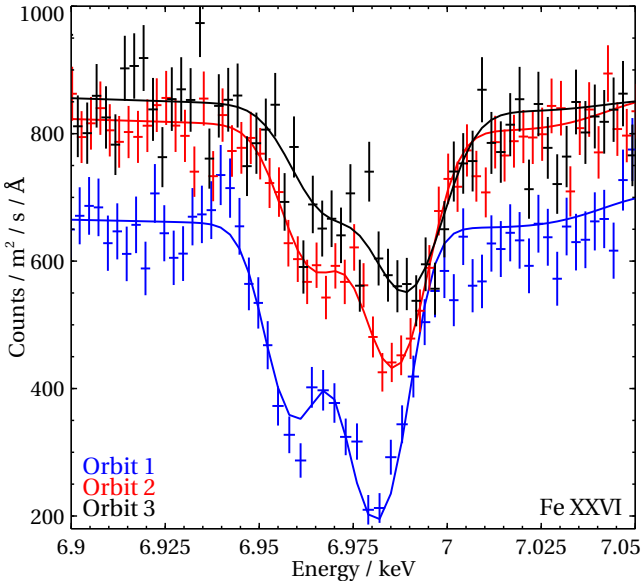

Figure 3. Comparison of the Fe XXVI region between the 3 Her X-1 high-flux orbits. Fe XXVI absorption originates in the disk wind, and clear variability is observed from orbit to orbit. The line optical depth decreases, and it becomes broader and shifts to higher energies, indicating that the wind increases in velocity as well as velocity width.

obtain a coverage from 1.8 to 75 keV which encompasses most of the X-ray emission of Her X-1 (more than 90% of its X-ray luminosity is in this range). The inclusion of the NuSTAR data is needed for correct spectral energy distribution (SED) modeling, necessary to apply a photoionization spectral model in Section 3.3, and also to correctly describe the primary continuum across a broad band. Incorrect primary continuum modeling could have consequences for the inference of best-fitting parameters of the highly broadened Fe K emission lines as well as of the absorption lines. As we did not observe any significant variability in the count rate (which agrees within 5%; Table 3) and spectral shape between the two NuSTAR observations taken during Orbit 2 and Orbit 3, for each time interval analyzed we use the full NuSTAR spectrum from the appropriate observation. We introduce a cross-calibration constant between the XRISM and NuSTAR data to account for any calibration differences and to account for possible residual variability from interval to interval in the hard X-ray ($>$12 keV) flux during individual XRISM intervals. The value of the cross-calibration constant varies by less than 10% for all analyzed intervals during Orbits 2 and 3 indicating weak, if any (pulse-averaged), variability in the hard X-rays.

For Orbit 1 intervals, which lack simultaneous NuSTAR coverage (due to a spacecraft tracker visibility violation at that time period), we use the NuSTAR observation from Orbit 2. The cross-calibration constant for the analyzed time intervals during Orbit 1 is on average 30% off the typical value during Orbits 2 and 3, indicating variability in the hard band. Nevertheless, inclusion of this (even if approximate) hard X-ray tail is much preferred to ignoring it completely. Assuming that the spectral shape in the hard X-ray band ($>$12 keV) remains consistent, the $\sim$30% flux variability is taken into account for SED modeling by applying the cross-calibration constant.

The primary continuum is described with a Comptonization component, using the COMT model. This model was found to be insufficient alone to describe the entire 1.8$-$75 keV energy band. A satisfactory fit was found when an additional hard exponential cutoff was applied using the ETAU component. The primary continuum is further affected by cyclotron resonance scattering at $\sim$35$-$40 keV (one of the most famous spectral features of Her X-1; J. Truemper et al. 1978), which we reproduce using a LINE component. This is a strictly phenomenological description of the primary X-ray pulsar emission which allows us to focus on the interpretation of the spectral features in the Fe K band.

We then focus on the Fe K band, which is shown in Figure 4. In agreement with our previous results from XMM-Newton (P. Kosec et al. 2022), we require two highly broadened emission lines to accurately describe the broad Fe K structure on which the narrow emission and absorption lines are imprinted. These lines are modeled with simple Gaussians, which describe the spectral shape required by the XRISM data surprisingly well. One of the lines has a 1σ width of about

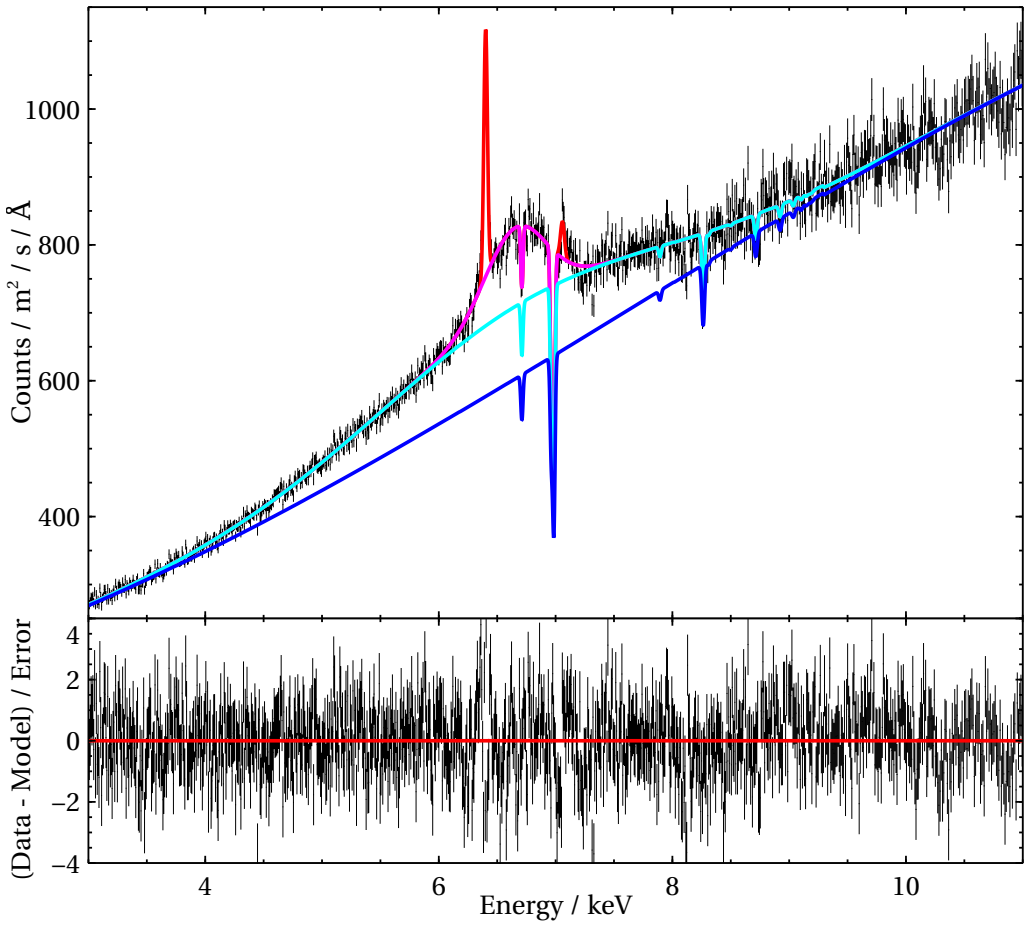

Figure 4. Time-averaged high-flux XRISM spectrum of Her X-1 (all three orbits combined), fitted with the phenomenological emission and absorption spectral model. The primary continuum is shown in blue. Two highly broadened emission lines are required in addition to the primary continuum for a satisfactory fit of the Fe K complex (blue and magenta). Narrow Fe I Kα and Kβ emission lines are shown in red. On top of this continuum model, we apply disk wind absorption (using the SLAB model in this example) which produces the narrow absorption lines across the Fe K band. The lower panel contains the residuals to the fit containing all spectral components.

1 keV and its centroid is consistent with Fe I at 6.4 keV, while the second line has a 1σ width of 0.2−0.3 keV and its centroid is instead consistent with the position of Fe XXV at 6.67 keV. The detailed properties of these features and their physical origin will be discussed in future work.

To describe the narrow Fe I Kα and Kβ lines, we also use single Gaussians. We note that we do not use two kinematic components to describe Fe I Kα and Kβ or the full Holzer line model (G. Hölzer et al. 1997) for these transitions in this work, as doing so would further increase the complexity of our model with very little effect on the absorber properties. As the origin of the two narrow lines is likely the same and the Kβ line is relatively weak, we couple its velocity width to that of the Kα component and couple its energy to that of the Kα component times the ratio of neutral Kβ and Kα rest-frame positions. The origin of the narrow Fe Kα and Kβ lines, and their multicomponent kinematic structure will be studied in detail in T. Narita et al. (2026, in preparation). Nevertheless, it is important to (at least crudely) model these features here for an accurate description of the emission continuum. Furthermore, the Fe I Kβ component is located at ∼7.07 keV, close to the Fe XXVI transition at 6.96 keV, and so omitting the Kβ model could have consequences for our description of the wind absorption through the Fe XXVI line. The time-averaged high-flux Her X-1 XRISM spectrum is shown in Figure 4 and shows how the final spectral model consists of different model components.

Finally, the entire Her X-1 emission spectrum is subjected to Galactic absorption. This is included within the model with a HOT component, which describes absorption by almost neutral gas (J. de Plaa et al. 2004). The column density of this absorber is set to $1 \times 10^{20}\,\mathrm{cm}^{-2}$ based on our previous study of Her X-1 (HI4PI Collaboration et al. 2016; P. Kosec et al. 2022). This Galactic absorption model is applied as the last effect, only after the ionized disk wind absorber is applied.

3.2. Phenomenological Wind Modeling

The aim of this study is to probe how the disk wind varies with the precession phase of Her X-1, as our sightline changes due to the warped disk precession. Therefore, we perform a detailed time-resolved study of the XRISM dataset. We chose a range of time-resolved intervals guided by the strength of the wind absorption lines and the statistics (and clean XRISM exposure) required to constrain them. As the first step, we perform phenomenological modeling of the wind absorption. We use the SLAB model (J. S. Kaastra et al. 2002) in SPEX, which can determine the ionic column density in any specific ion by simultaneously fitting the optical depth of all the absorption lines which such ion produces. At the same time, the ratios of the different ion column densities are not

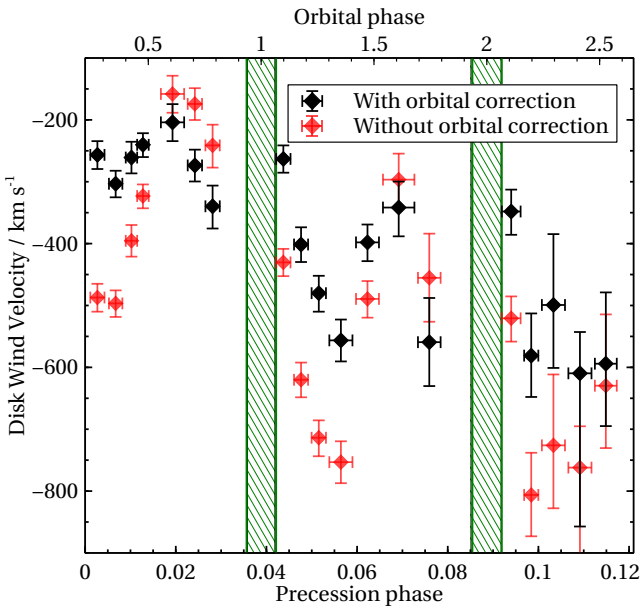

Figure 5. Disk wind velocity versus Her X-1 precession phase and orbital phase. The best-fitting velocity with no corrections applied is in red. Clear orbital motion is observed in the evolution of this velocity. In black, we show the velocity evolution after correcting for the orbital motion of the neutron star. Her X-1 eclipses by the secondary star are shown with green horizontal lines.

constrained, and as such this spectral model gives us the most model-independent understanding of how the wind absorption lines behave over time.

The strongest features of the disk wind in the 2−10 keV XRISM bandpass are the absorption lines of Fe XXV and Fe XXVI. In this first step, we simply use SLAB to fit for the column density of Fe XXV and XXVI ions. The SLAB model has two further variables: the absorber velocity (determined from the blueshift of the component) and the velocity width (determined from the line widths). This basic setup allows us to investigate any variation in the wind kinematics and in the strength of its wind absorption signatures.

XRISM has the capability to track the kinematics of the wind of Her X-1 and its variations despite the low wind velocity of just hundreds of km s^{-1}. We observe that the wind velocity evolves in a range between 150 and 800 km s^{-1}. This is consistent with previous X-ray grating measurements in Her X-1 using Chandra HETG and XMM-Newton RGS (P. Kosec et al. 2020, 2023a, 2023b). In fact, the XRISM data quality is so good that we can now observe binary orbital motion in the evolution of the wind velocity with the precession phase. This is shown in Figure 5 by using the densest time-resolved sampling attempted in this study, where we split the high-flux XRISM exposure from all three orbits into 19 time intervals. Clear sinusoidal motion is observed on the timescale of the orbital period, which is expected because the wind is launched by the accretion disk orbiting the neutron star, and the neutron star is in orbital motion with the secondary star. On top of the orbital evolution, we also see systematic evolution in wind outflow velocity with the precession phase.

In the following analysis, we correct any wind outflow velocity measurements for the orbital motion of the neutron star and its accretion disk. We use the velocity correction formula from P. Kosec et al. (2020), based on the measurement of the projected orbital velocity of 169.049 ± 0.004 km s^{-1} by J. E. Deeter et al. (1981) and the systemic velocity of Her X-1 of −65 ± 2 km s^{-1} by A. P. Reynolds et al. (1997). The orbital phase was calculated using the ephemeris of R. Staubert et al. (2016), which specifies an orbital period of 1.700167590 days, an eclipse midpoint on MJD 46359.871940, and a change in the orbital period of $-(4.85 \pm 0.13) \times 10^{-11}$ s s^{-1}.

We experimented with a range of time interval splitting which would maximize the time resolution while minimizing the uncertainties on the relevant parameters. In the end, a compromise was achieved by splitting the high-flux XRISM exposure into 14 intervals, where the exposure of each interval varied adaptively depending on the strength of the Fe XXV and XXVI wind absorption during each interval. The SLAB component free parameters were measured for each analyzed interval. The results are shown in Figure 6 and listed in Table 1. We find that the wind is strongly variable, in agreement with previous studies, and that all four SLAB parameters vary significantly over the sampled precession phase range. Additionally, the observed variations are not monotonic in most of the parameters, but show jumps just after Her X-1 emerges from eclipses by the secondary. We discuss these results in Section 4.

3.3. Photoionization Wind Modeling

In the second part of the analysis, we replace the phenomenological SLAB model with the photoionization model PION (M. Mehdipour et al. 2016) while keeping the other (continuum) spectral components the same. PION takes into account the SED of the currently loaded emission spectral model to calculate the ionization balance of all elements and produce their transmission function when subjected to the input SED, assuming photoionization equilibrium. Therefore, with PION we can take into account all of the wind absorption lines across the XRISM energy range, but at much higher computational cost. In return, we are able to determine physical parameters of the outflow such as its column density and ionization parameter, required to determine the outflow energetics and mass outflow rate. This is also naturally a more model-dependent approach to analyzing the wind properties than using the phenomenological SLAB model which does not make assumptions on the conditions of the wind (e.g., single ionization phase versus multiphase), which is why we describe the results from both approaches in this manuscript.

PION requires correct SED modeling to accurately determine the physical quantities. This is one of the main reasons why we add NuSTAR data to any XRISM time interval spectral fit. To also model the soft X-rays (0.35–1.8 keV) accurately, we perform a spectral fit of the RGS data from XMM-Newton which was taken simultaneously with Orbits 1 and 3. For this step, the RGS data are used solely to determine the shape of the SED and not to constrain any of the wind absorption lines in the RGS band, considering we only have partial time coverage of the XRISM observations with XMM-Newton. The RGS data are fitted with a simplified model from Appendix B containing a simple blackbody (BB), a blackbody modified by coherent scattering (MBB), and one Gaussian line describing the broad 1 keV feature (detailed reasoning for these specific model components is in P. Kosec et al. 2022). This simplified model accounts for more than 99% of the soft X-ray flux. The model is added to each fitted XRISM time interval, and its best-fitting parameters (from the RGS analysis) are fixed. For all time intervals during Orbit 1, we

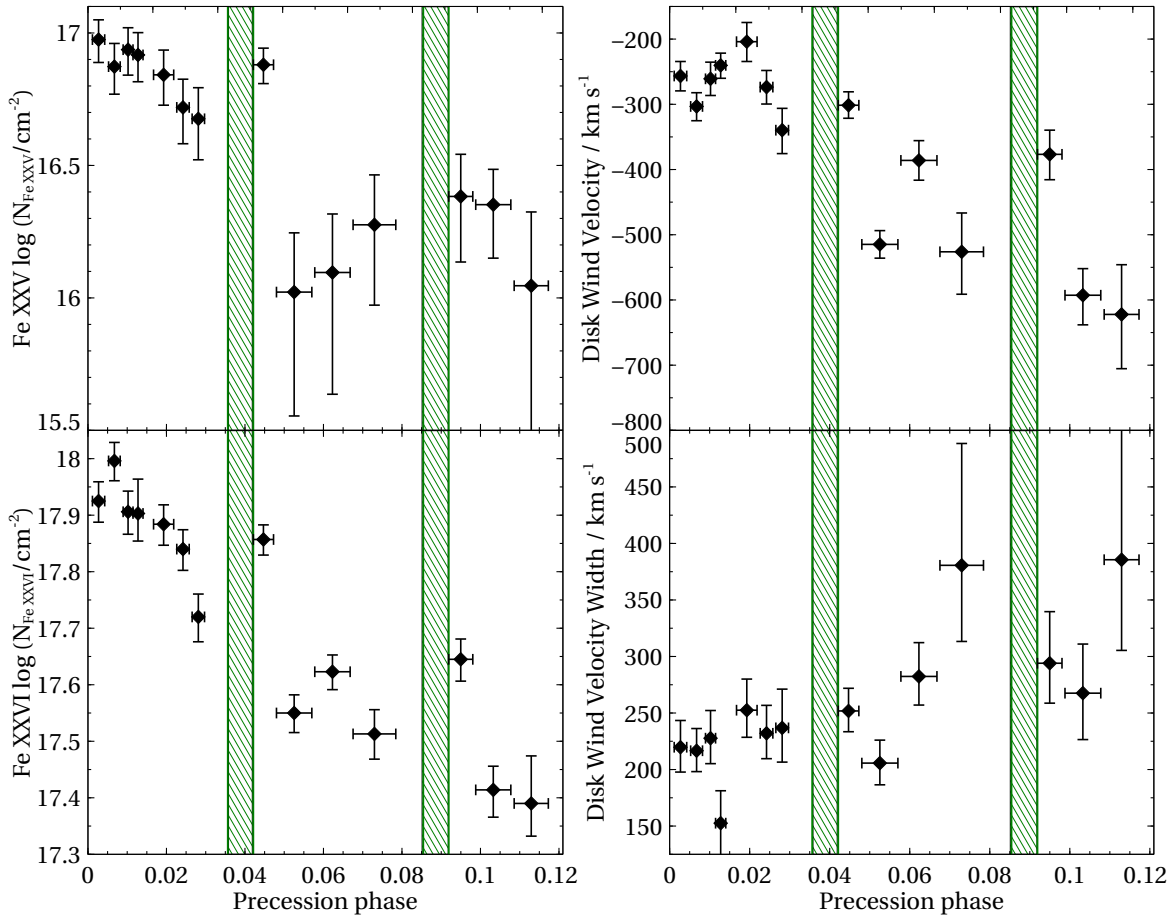

Figure 6. Time-resolved phenomenological analysis of the disk wind properties using the SLAB model. The two panels on the left show the best-fitting ionic column densities of Fe XXV (top) and Fe XXVI (bottom). The two panels on the right show the kinematics of the wind (assuming the same kinematics for both lines), its outflow velocity (top), and the velocity width (bottom). The green vertical lines with shading indicate the Her X-1 eclipses.

Table 1
Results of the Phenomenological Disk Wind Analysis Using the SLAB Model

Orbit	Seg.	Precession Phase	Fe XXV Column Density $\log(N_{Fe\ XXV}/cm^{-2})$	Fe XXVI Column Density $\log(N_{Fe\ XXVI}/cm^{-2})$	Outflow Velocity (km s^{-1})	Velocity Width (km s^{-1})	C-stat/D.o.F.
1	S1	0.00270 ± 0.00156	$16.98^{+0.075}_{-0.086}$	$17.92^{+0.04}_{-0.05}$	-260^{+20}_{-30}	220^{+30}_{-20}	5563.4/5474
	S2	0.00673 ± 0.00148	$16.87^{+0.087}_{-0.10}$	$18.00^{+0.04}_{-0.04}$	-300^{+20}_{-20}	220^{+20}_{-20}	5862.4/5495
	S3	0.01022 ± 0.00126	$16.94^{+0.083}_{-0.096}$	$17.91^{+0.04}_{-0.04}$	-260^{+30}_{-30}	230^{+30}_{-30}	5824.6/5454
	S4	0.01275 ± 0.00128	$16.92^{+0.084}_{-0.10}$	$17.90^{+0.06}_{-0.05}$	-240^{+20}_{-20}	150^{+30}_{-40}	5928.9/5488
	S5	0.01928 ± 0.00257	$16.84^{+0.093}_{-0.11}$	$17.88^{+0.04}_{-0.04}$	-200^{+30}_{-30}	250^{+30}_{-30}	5729.6/5545
	S6	0.02421 ± 0.00158	$16.72^{+0.11}_{-0.14}$	$17.84^{+0.04}_{-0.04}$	-270^{+30}_{-30}	230^{+30}_{-20}	5698.2/5647
	S7	0.02812 ± 0.00158	$16.68^{+0.12}_{-0.15}$	$17.72^{+0.04}_{-0.05}$	-340^{+40}_{-40}	240^{+40}_{-30}	5737.1/5622
2	S8	0.04470 ± 0.00258	$16.88^{+0.063}_{-0.071}$	$17.86^{+0.03}_{-0.03}$	-300^{+20}_{-20}	250^{+20}_{-20}	6240.7/5943
	S9	0.05253 ± 0.00451	$16.02^{+0.22}_{-0.47}$	$17.55^{+0.03}_{-0.04}$	-510^{+20}_{-20}	210^{+20}_{-20}	6228.4/6135
	S10	0.06229 ± 0.00451	$16.10^{+0.22}_{-0.46}$	$17.62^{+0.03}_{-0.03}$	-390^{+30}_{-30}	280^{+30}_{-30}	6284.4/6115
	S11	0.07299 ± 0.00544	$16.28^{+0.19}_{-0.30}$	$17.51^{+0.05}_{-0.05}$	-530^{+60}_{-70}	380^{+110}_{-70}	6273.3/6131
3	S12	0.09498 ± 0.00307	$16.38^{+0.16}_{-0.25}$	$17.65^{+0.04}_{-0.04}$	-380^{+40}_{-40}	290^{+50}_{-40}	6176.6/5986
	S13	0.10326 ± 0.00447	$16.35^{+0.13}_{-0.20}$	$17.41^{+0.04}_{-0.05}$	-590^{+40}_{-50}	270^{+50}_{-40}	6228.6/6136
	S14	0.11294 ± 0.00435	$16.05^{+0.28}_{-0.81}$	$17.39^{+0.09}_{-0.06}$	-620^{+80}_{-90}	390^{+260}_{-80}	6500/6124

use the results from the XMM-Newton observation taken during that orbit. For all time intervals during Orbits 2 and 3, we use results from the XMM-Newton observation taken concurrently with Orbit 3, considering that Orbits 2 and 3 show comparable count rates across the XRISM energy band (while Orbit 1 is somewhat fainter; Figure 1). An example of the final, full-band SED (from Orbit 1) is shown in Figure 9.

Additionally, PION assumes elemental abundances during the spectral fit. These could in principle be left to the default (Solar) values. However, there is strong evidence suggesting

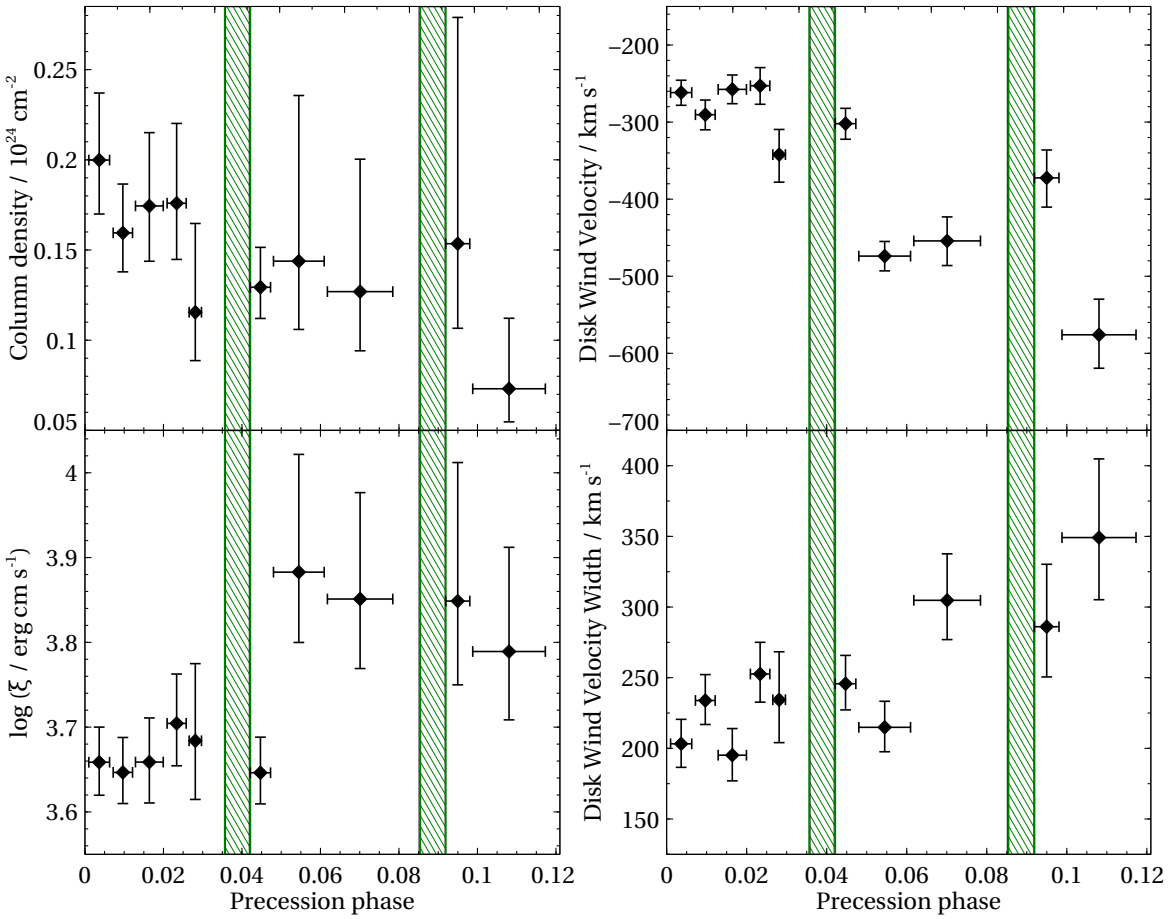

Figure 7. Time-resolved physical photoionization analysis of the disk wind properties. The two panels on the left show the best-fitting disk wind column density $N_{\rm H}$ (top) and its ionization parameter $\log(\xi/\mathrm{erg\ cm\ s^{-1}})$ (bottom), and the two panels on the right show the kinematics of the wind, its outflow velocity (top), and the velocity width (bottom). The green vertical lines with shading indicate the Her X-1 eclipses.

that elemental ratios in Her X-1 are in fact not Solar (M. A. Jimenez-Garate et al. 2002, 2005; P. Kosec et al. 2023a, 2023b). Therefore, before proceeding with the time-resolved PION analysis, we perform the best-quality analysis of the wind elemental abundances given our simultaneous coverage with XMM-Newton and XRISM that cover a wide energy band (0.35–12 keV), containing a broad range of elemental transitions. This elemental abundance analysis is described in further detail in Appendix B. In the PION analysis described below, we fix the abundances to the values listed in Table 6.

The derived SEDs and elemental abundances are applied in a spectral fit to each of the time intervals independently. For this analysis, we had to reduce the number of time intervals to just 10. This was needed because PION requires multiple ionic transitions to accurately determine the column density and the ionization parameter—specifically, both Fe XXV and XXVI absorption lines are required—and the Fe XXV line is much weaker than the Fe XXVI line. Increasing the number of time intervals significantly expanded the uncertainty ranges on the column density and ionization parameter. The results of the PION analysis are shown in Figure 7 and listed in Table 2, and the individual segment spectra focusing on the Fe XXV and XXVI energy bands are shown in Figure 8 in Appendix A. As in the phenomenological analysis with the SLAB model, all parameters strongly vary with Her X-1 precession phase. The results are discussed in the following section.

4. Discussion

We perform a comprehensive time-resolved analysis of the disk wind of Her X-1 by analyzing a long observation by XRISM. The total duration of ∼380 ks allows us to probe the wind properties for a significant fraction of the Main High state, spanning roughly 12% of the entire 35 day precession period. The disk precession during this time shifts our line of sight across the wind vertical structure, resulting in a range of X-ray absorption spectra which give us a unique insight into the vertical properties of this structure. The observational campaign led by XRISM and supported by coordinated observations with XMM-Newton, NuSTAR, and Chandra also spanned almost three full high-flux (Main High state) orbital periods of Her X-1 and additionally captured three eclipses, three periods of absorption dips, and a brief period of Low state. While this manuscript focuses on the measurement of time-resolved wind properties, our future publications will study many other aspects of this dataset including the pulse-resolved wind behavior, Her X-1 emission lines, and other flux states.

For the first time, thanks to the spectral resolving power of XRISM we are able to completely resolve the complex Fe K band of Her X-1. P. Kosec et al. (2022) correctly identified several features in this energy band including the disk wind absorption lines (the strongest being the Fe XXV and Fe XXVI lines), a narrow Fe Kα line, a broadened Fe XXV line, and a highly broadened Fe K line. However, only now it is possible

Table 2
Results of the Photoionization Disk Wind Analysis Using the PION Model

Orbit	Seg.	Precession Phase	Column Density (10^{24} cm^{-2})	$\log(\xi/\mathrm{erg\ cm\ s^{-1}})$	Outflow Velocity (km s^{-1})	Velocity Width (km s^{-1})	C-stat/D.o.F.
1	P1	0.00363 ± 0.00264	$0.200^{+0.037}_{-0.030}$	$3.66^{+0.04}_{-0.04}$	-262^{+16}_{-17}	203^{+17}_{-17}	6009.7/5707
	P2	0.00966 ± 0.00247	$0.159^{+0.027}_{-0.022}$	$3.65^{+0.04}_{-0.04}$	-290^{+19}_{-20}	234^{+18}_{-17}	6137.6/5822
	P3	0.01641 ± 0.00354	$0.174^{+0.041}_{-0.031}$	$3.66^{+0.05}_{-0.05}$	-258^{+19}_{-19}	195^{+19}_{-18}	5894.2/5618
	P4	0.02336 ± 0.00243	$0.176^{+0.044}_{-0.031}$	$3.70^{+0.06}_{-0.05}$	-253^{+24}_{-24}	253^{+22}_{-20}	5946.1/5831
	P5	0.02811 ± 0.00157	$0.116^{+0.049}_{-0.027}$	$3.68^{+0.09}_{-0.07}$	-342^{+33}_{-36}	234^{+34}_{-30}	5734/5622
2	P6	0.04470 ± 0.00258	$0.129^{+0.022}_{-0.017}$	$3.65^{+0.04}_{-0.04}$	-302^{+20}_{-20}	246^{+20}_{-19}	6237.9/5943
	P7	0.05449 ± 0.00646	$0.144^{+0.092}_{-0.038}$	$3.88^{+0.14}_{-0.09}$	-474^{+19}_{-19}	215^{+18}_{-17}	6419.5/6438
	P8	0.07010 ± 0.00833	$0.127^{+0.073}_{-0.033}$	$3.85^{+0.13}_{-0.08}$	-454^{+31}_{-32}	305^{+33}_{-28}	6761.2/6573
3	P9	0.09498 ± 0.00307	$0.153^{+0.130}_{-0.047}$	$3.85^{+0.16}_{-0.10}$	-372^{+36}_{-38}	286^{+44}_{-36}	6176/5986
	P10	0.10804 ± 0.00925	$0.073^{+0.039}_{-0.018}$	$3.79^{+0.12}_{-0.08}$	-576^{+46}_{-43}	349^{+56}_{-44}	7061.7/6796

to measure the properties of these individual features with confidence.

4.1. Evolution of the Disk Wind with Precession Phase

The time-resolved analysis shows that all parameters of the wind are strongly variable. We clearly observe the imprint of the Her X-1 binary orbital motion on the projected wind velocity (Figure 5), showcasing the impressive performance of XRISM. Binary orbital motions were also recently detected with XRISM/Resolve in other X-ray binaries including Cen X-3 by Y. Mochizuki et al. (2024) and in Cyg X-3 by XRISM Collaboration et al. (2024) and D. Miura et al. (2025). Even after correcting for the orbital motion effect, the Her X-1 projected outflow velocity systematically increases over time from 250 to 600 km s^{-1}, as the precession phase increases and our line of sight samples greater heights of the wind above the warped disk. Neither the orbital motion nor this systematic velocity evolution was previously detected with XMM-Newton or Chandra (see, e.g., Extended Data Figure 4 of P. Kosec et al. 2023a).

The observation of an increasing velocity could indicate that the total wind velocity increases as the wind rises above the disk—in other words, the wind is still within the acceleration zone as it is sampled by our sightlines. Alternatively, at least its projected velocity must increase, i.e., as it rises higher above the disk, its velocity vector aligns more with our line of sight. In reality, both of these possibilities may be at play. The detection of an accelerating outflow would be of importance for determining the launching mechanism considering that thermally launched winds are ballistic, with no significant acceleration expected above the disk (M. C. Begelman et al. 1983). The detection of an accelerating motion would therefore indicate a magnetic origin of the wind, considering the relatively low Eddington fraction of Her X-1 (0.1−0.2) and the high ionization of the wind (likely excluding purely radiatively launched outflows). Therefore it is crucial to determine if the wind is indeed accelerating, or its streamlines are only being projected more along our line of sight as it rises higher above the disk.

In addition to the varying outflow velocity, we also observe a monotonic increase in the velocity width of the wind absorption lines from 200 to 400 km s^{-1}. This is unlikely to be due to an increase in thermal turbulent velocity (as the wind ionization parameter and temperature do not greatly increase over time), but instead is plausibly due to a range of streamlines crossing our line of sight, which all have a slightly different projected outflow velocity from our line of sight. If the velocity vectors of these streamlines diverge going upwards in the flow, the line velocity width will increase as our sightline moves to greater heights. Additionally, as each time interval has a definite exposure time, the Her X-1 orbital velocity change over this exposure duration will also contribute to the velocity width of the observed (time-integrated) wind features. However, this effect should not form the majority of the line velocity width, as the SLAB and PION analyses use different time interval samplings and still show consistent velocity widths.

The column density of the wind, either in the individual lines (Figure 6) or in the overall $N_{\rm H}$ (Figure 7), is seen to decrease significantly over time. Particularly, the Fe XXVI transition appears to decrease almost linearly over time from $10^{18.0}$ cm^{-2} down to $10^{17.4}$ cm^{-2}, with two exceptions (discussed below). However, the change in the overall $N_{\rm H}$ of the wind (from the PION analysis) from 2×10^{23} cm^{-2} down to 7×10^{22} cm^{-2} is not as sharp as in P. Kosec et al. (2023a) where a variation of as much as 3 orders of magnitude was found. Here, the change appears to be much lower by about a factor of 3. This is because the behavior of the ionization parameter is very different compared with the previous analysis using XMM-Newton data. Instead of strongly decreasing over time as seen in P. Kosec et al. (2023a), $\log(\xi/\mathrm{erg\ cm\ s^{-1}})$ is relatively stable in Orbit 1 at around a value of 3.65−3.7 and increases in Orbits 2 and 3 to values consistent with 3.8−3.9. There appears to be a step change in the ionization parameter after the first data point during Orbit 2 in the PION analysis (Figure 7); however, it is likely that the best-fitting $\log(\xi/\mathrm{erg\ cm\ s^{-1}})$ value of that data point is affected by the possible presence of a multiphase absorber structure along our line of sight during that time segment (discussed in the next subsection). The accretion disk wind $\log(\xi/\mathrm{erg\ cm\ s^{-1}})$ variation may thus be smoother than is apparent from Figure 7, but in each case the variation in this parameter over the 2024 XRISM campaign is very limited in comparison with previous measurements.

One possibility is that the difference in the $\log(\xi/\mathrm{erg\ cm\ s^{-1}})$ evolution between the XRISM and the older XMM-Newton and Chandra observations is due to the great improvement in the dataset quality in the Fe K energy band

thanks to the spectral resolution of Resolve (Figure 2). Archival RGS observations (e.g., Extended Data Figure 1 in P. Kosec et al. 2023a) show a decrease in the strength of the N, O, and Ne Lyα lines with the precession phase. This can be explained either by a strong decrease in the column density or an increase in the ionization parameter (or by a combination of both these variations). However, measuring the Lyα lines and their ratios in the RGS energy band is not sufficient to accurately measure the ionization of the wind. At these ionization parameters, $\log(\xi/\mathrm{erg\ cm\ s^{-1}})$ is primarily constrained by the ratio of the Fe XXV and Fe XXVI transitions, which are poorly resolved in the archival XMM-Newton EPIC data. The Fe XXV line is particularly weak, as can also be seen in the present XRISM study. The spectral fits based on EPIC data could then be affected by a degeneracy between the strength of the broadened Fe XXV emission line at 6.67 keV and the optical depths of the Fe XXV and Fe XXVI wind absorption lines (see also Appendix B for a further discussion of this effect). One piece of supporting evidence for this hypothesis is that at low Her X-1 precession phases (phases 0 −0.04)—when the wind absorption lines are strong—the measurements by XRISM (Figure 7) are in agreement with those by XMM-Newton and Chandra (Figure 2 in P. Kosec et al. 2023a). The measurements only significantly begin to diverge at greater precession phases (phase > 0.05) when the wind features weaken.

An alternative possibility is that the wind structure has evolved since it was previously observed with XMM-Newton and Chandra (during the large campaign in 2020 and before), and the differences between the parameter evolutions are real. Indeed, some change in the wind parameters is probably not unlikely. However, it is not clear if the evolution of the ionization parameter with the precession phase could invert completely based on such changes. This would be of great interest as it would suggest that the disk wind of an X-ray binary can significantly evolve without an apparent change in any other relevant parameters such as the intrinsic source luminosity. In any case, both the current XRISM as well as the previous XMM-Newton/Chandra observations agree that the wind absorption lines weaken with increasing precession phase.

Ultimately, now we can finally measure the ionization parameter with accuracy thanks to XRISM/Resolve. These measurements indicate (at least for this specific 35 day cycle) that as the wind rises to greater height above the disk, its ionization increases and potentially stagnates. This is consistent with the wind "freezing out" at a constant $\log(\xi/\mathrm{erg\ cm\ s^{-1}})$ as it rises and expands into 3D space. A $\log(\xi/\mathrm{erg\ cm\ s^{-1}})$ stagnation would indicate that the wind number density evolves as $n \sim R^{-2}$ as it expands into space considering the ionization parameter definition of $\xi = L/(nR^2)$, where L is the ionizing flux, n is the wind number density, and R is its distance from the ionization source. However, further XRISM observations at later Her X-1 precession phases would be necessary to confirm this potential trend, as well as definitively answer if the wind structure evolves over different 35 day cycles.

We note that the observed Her X-1 flux slightly increases over the XRISM observation, which can be seen in the increasing count rate in Figure 1, by about 20% between Orbit 1 and Orbit 2. However, this flux increase is insufficient to cause the observed increase in the value of the ionization parameter. Considering the definition of $\log(\xi/\mathrm{erg\ cm\ s^{-1}})$ (assuming a change in flux only, with no variation in number density and location), the Her X-1 flux would have to increase by 60% to explain the observed $\log(\xi/\mathrm{erg\ cm\ s^{-1}})$ variation by $\sim$0.2.

The different $\log(\xi/\mathrm{erg\ cm\ s^{-1}})$ variation with the precession phase inferred here has implications for the 2D map of the wind produced in our previous work (P. Kosec et al. 2023a). Qualitatively, this change in the ionization parameter evolution will push the wind location estimates (at certain phases/heights) with respect to the wind base closer to the neutron star. Hence, the wind streamline will be oriented more vertically than shown in Figure 4 of P. Kosec et al. (2023a).

We note that the significant uncertainties on the values of the column density are due to a degeneracy between N_{H} and $\log(\xi/\mathrm{erg\ cm\ s^{-1}})$. The uncertainties on $\log(\xi/\mathrm{erg\ cm\ s^{-1}})$ are introduced because of the weakness of the Fe XXV transition, particularly in the second half of our campaign. This does not mean that the wind is detected weakly in these time segments, as it is still strongly detected through the Fe XXVI transition (Figure 6). In each of the individual segments, the statistical improvement upon adding the disk wind is at least ΔC-stat of 90, but typically reaches 200−500.

We also use this combined X-ray dataset to measure the elemental abundances in the disk wind of Her X-1. This is discussed in further detail in Appendix B and the best-fitting abundances are listed in Table 6. In summary, the abundances of elements primarily in the RGS band (N and Ne) are overabundant compared with O and consistent with previous studies (P. Kosec et al. 2023a). However, the Fe/O ratio is significantly different from the previously measured value of 2.3 due to our improved spectral resolution in the Fe K band and is $0.70^{+0.08}_{-0.10}$.

In addition to modeling the wind ionized absorption, we also searched for re-emission from the regions of the outflow that are not along our line of sight. The detection of emitting wind plasma would help constrain its solid angle and the 3D wind structure in even more detail. This re-emission is very weak, even in the high-quality XRISM data. It is completely absent in the time-averaged high-flux spectrum (Figure 2). There is evidence for weak re-emission in the orbit-resolved XRISM data, but only in Orbit 1 (Figure 3). This indicates that the outflow is being launched into a small solid angle, consistent with X-ray binary disk wind population studies (G. Ponti et al. 2012; M. Parra et al. 2024).

The large coordinated observational campaign on Her X-1 led by XRISM and supported by XMM-Newton, NuSTAR, and Chandra reveals the structure of its accretion disk wind in unprecedented detail. This first study of the 2024 dataset where we performed a time-resolved, pulse-averaged study of the wind shows how the structure changes upwards along the wind streamlines, as the precessing disk moves our sightline to consecutively greater heights above the disk. At the same time, the depth of this study only scratches the surface that the XRISM data provide and opens many new questions discussed above. A follow-up study (P. Kosec et al. 2026, in preparation) will explore the pulse-resolved variability of the wind properties, which has the power to constrain the wind number density via time-dependent photoionization modeling (P. Kosec et al. 2024) and precisely locate it along our line of sight to the neutron star. In future work, we will also

produce an updated 2D map of the disk wind (P. Kosec et al. 2023a), taking into account the new XRISM measurements, and directly compare the wind parameter measurements and their evolution with the precession phase (and height above the disk) with a range of hydrodynamical simulations assuming various disk-wind-driving mechanisms. Using this comparison, we will additionally address the question of the evolving wind velocity to answer whether the wind is still located within the acceleration zone or if only its projected velocity increases as it follows the streamlines and rises higher above the accretion disk.

The projected wind outflow velocity is seen to increase along the wind streamlines, from 250 to 600 km s^{-1}. The question is as follows: how much more can it increase further up the flow? If the wind is indeed thermally driven, a terminal velocity exceeding 1000 km s^{-1} would require very high Compton temperatures to accelerate the outflow to such speeds, or alternatively a contribution from radiation pressure would be needed. Future Her X-1 observations with XRISM at even later Her X-1 precession phases would help to answer this question and allow us to understand the wind properties even further along the streamlines, as the wind continues expanding into 3D space.

4.2. Wind Parameter Variations with Orbital Phase—Evidence for a Second Wind Component?

Most of the wind parameter evolution (after accounting for orbital motion) appears relatively smooth and monotonic, with two major exceptions. After each eclipse by the secondary, most wind parameters significantly jump. This is seen particularly in the Fe XXV and XXVI line column densities in Figure 6, which strongly increase for a single time segment. A similar shift is also observed in the outflow velocity (in both the SLAB and PION analyses). Surprisingly, no similar variability is seen in the velocity width, which remains consistent across the eclipses in both analyses. At the same time, no jumps in any wind parameters are seen just before the eclipses. However, we note that we lack coverage immediately preceding the eclipses, as these intervals are affected by pre-eclipse absorption dips (not analyzed in this study), which offer limited information on the wind properties (Figure 1) given the much lower count statistics.

The observed jumps indicate a more complex nature of the disk wind than previously considered, showing behavior that was not seen in XMM-Newton or Chandra observations of Her X-1. The jumps clearly show dependence on the orbital phase, and the large changes seem to only occur immediately following an eclipse, when our line of sight passes close to the secondary star. This may indicate the multiphase nature of the wind, with one component originating from the Her X-1 accretion disk and following a smooth evolution (seen particularly in the Fe XXVI line column density), and a second component, plausibly originating from the secondary star (considering the orbital phase dependence) and only appearing over a specific range of orbital phases. We note that if there are indeed two absorber components, our PION analysis may be affected in the two data points immediately following the eclipses as it strictly assumes one component with a single ionization parameter $\log(\xi/\mathrm{erg\ cm\ s^{-1}})$. If two components are present with different ionization parameters, the best-fitting single PION model parameters will be biased. This would explain why the SLAB ionic column density jumps for both Fe XXV and XXVI after the first eclipse but the same does not occur for the overall PION column density.

In the case of two wind components with slightly different projected outflow velocities causing the jumps in the absorber systematic velocity, we would in principle also expect an increase in the absorber velocity width. This is surprisingly not observed, but it could again be an artifact of the fitting process driven by the usage of a single kinematic model, or a limitation of the dataset even with the resolution power of XRISM/Resolve.

One of the possible launching mechanisms for this outflow, if it is launched from the secondary star, may be the strong X-ray illumination of the secondary by Her X-1, which could launch a thermal wind from the stellar surface. The existence of such a wind was previously hypothesized by B. Boroson et al. (2001) based on the detection of P-Cygni profiles in the UV band. However, we note that these UV line detections in Her X-1 predate most X-ray binary disk wind confirmations (in the X-rays) and particularly the disk wind detection in this source (P. Kosec et al. 2020). It is thus possible that the UV lines are imprinted instead by the accretion disk wind. A reanalysis of the original HST observations from B. Boroson et al. (2001) could inform us of their relation to the absorber observed in the X-ray band.

An alternative possibility is that there is a single disk wind component with its streamlines focused by the secondary star's gravity, the effect of which is only observable close to the eclipses. However, the previous estimates of the wind's distance from the X-ray source all place the wind location within the outer accretion disk radius, far away from the stellar influence. A more complex spectral analysis containing multiple absorption zones is required. This will be explored in follow-up work.

5. Conclusions

We present the first results from a large coordinated campaign on Hercules X-1 led by XRISM (210 ks exposure) and supported by XMM-Newton (80 ks), NuSTAR (40 ks), and Chandra (50 ks). This work focuses on the properties of the vertical structure of the disk wind of Her X-1, which we measured by performing a time-resolved analysis of the observations. We applied both phenomenological as well as physical spectral models to describe the ionized absorption imprinted by the outflow. Our conclusions are as follows:

1. For the first time, thanks to the excellent spectral resolution of XRISM, we are able to fully resolve the complex Fe K energy band of Her X-1, and accurately measure the properties of the individual components. In particular, the absorption lines of Fe XXV and Fe XXVI from the accretion disk wind are resolved and allow us to accurately measure the ionization parameter of the wind.
2. We directly observe the orbital motion of Her X-1 in the evolution of the wind outflow velocity. After correcting for this motion, the wind velocity is seen to increase with rising precession phase from 250 to 600 km s^{-1}, as our sightline progressively samples the wind streamlines at greater heights above the disk. This indicates that either the wind is still within the acceleration zone at these heights, or that its velocity vector progressively aligns with our line of sight with increasing height above the

disk. Additionally, we also observe a rise in the wind velocity width with increasing precession phase, from 200 to 400 km s^{-1}.

3. The column density of the wind decreases with increasing height above the disk, in agreement with previous observations, from 20×10^{22} to 7×10^{22} cm^{-2}. This decrease is also observed in the individual Fe XXV and XXVI absorption lines. In contrast to previous results, the ionization parameter $\log(\xi/\mathrm{erg\ cm\ s^{-1}})$ increases with the precession phase, from 3.65 to 3.8−3.9, and stagnates around this value as the wind expands into 3D space.
4. The wind parameter evolution is relatively smooth throughout the observation, except immediately after each eclipse, when a significant increase in ionized absorption is observed. We also detect a jump in the wind velocity at these phases. This suggests that the ionized absorption is multiphase, and a second component appears only briefly after eclipses. The second component may originate from the secondary star and could be driven thermally by the strong illumination of the secondary by the intense X-ray radiation from Her X-1.
5. The improved spectral data quality allows us to perform a thorough study of elemental abundances within the disk wind. We are able to constrain the abundances of C, N, O, Ne, Mg, Si, S, Ar, Ca, Fe, and Ni. Their best-fitting values are listed in Table 6.

Acknowledgments

Support for this work was provided by NASA through the NASA Hubble Fellowship grant HST-HF2-51534.001-A awarded by the Space Telescope Science Institute, which is operated by the Association of Universities for Research in Astronomy, Incorporated, under NASA contract NAS5-26555. P.K. also acknowledges support from NASA grants 80NSSC25K7317 and 80NSSC25K7533. C.P. is supported by European Union—Next Generation EU, Mission 4 Component 1 CUP C53D23001330006. D.J.W. acknowledges support from the Science and Technology Facilities Council (STFC; grant code ST/Y001060/1). This paper employs a list of Chandra datasets, obtained by the Chandra X-ray Observatory, contained in the Chandra Data Collection doi:10.25574/cdc.569.

Facilities: XRISM, XMM, NuSTAR, CXO.

Software: Veusz, SPEX (J. S. Kaastra et al. 1996), XSPEC (K. A. Arnaud 1996).

Appendix A
Further Details of Individual Observations and Time-resolved Data Intervals

Table 3 contains details about all coordinated observations during the 2024 campaign on Her X-1. We explored a range of segmenting approaches by splitting the XRISM dataset into 10 intervals (used in the PION analysis in Section 3.3), 14 intervals (used in SLAB analysis in Section 3.2), and 19 intervals (used for the velocity evolution; Figure 5). The details in Table 4 are given for the 14 segment approach and in Table 5 for the 10 segment approach. Both tables include the clean exposure and the mean Hp and Mp quality event count rate of each segment as well as the segment center points in MJD and in Her X-1 precession phase. Figure 8 contains the narrow-band XRISM spectra from the 10-segment analysis (focusing on the Fe XXV and XXVI energy region) including the best-fitting PION spectral model.

Table 3
Details of all Observations during the 2024 Coordinated Campaign on Her X-1

Observatory	Observation ID	Start Time	End Time	Instrument	Exposure (s)	Count Rate (s^{-1})
XRISM	201074010	2024-09-10 02:19	2024-09-14 10:46	Resolve	144,451	16.7
NuSTAR	81002350002	2024-09-11 21:51	2024-09-12 08:51	FPMA	17,953	62.4
				FPMB	18,024	58.5
NuSTAR	81002350004	2024-09-13 13:51	2024-09-14 00:56	FPMA	18,120	63.2
				FPMB	18,192	59.0
XMM-Newton	0953011401	2024-09-10 20:55	2024-09-11 13:34	RGS 1	37,552	8.64
				RGS 2	37,290	9.56
XMM-Newton	0953011501	2024-09-13 17:18	2024-09-13 22:52	RGS 1	18,270	11.0
				RGS 2	18,162	12.1
Chandra	28768	2024-09-10 07:53	2024-09-10 09:33	MEG	5980.8	5.02
				HEG	5980.8	3.47
Chandra	29528	2024-09-11 23:08	2024-09-12 07:24	MEG	27,518	7.11
				HEG	27,518	4.91

Note. The exposure value is the clean exposure from all intervals of high flux after excluding all periods of time during which Her X-1 was exhibiting Low state, eclipses, and absorption dips.

Table 4
Details of Time-resolved XRISM Analysis, where All High-flux Periods of Time Were Split into 14 Segments, Used in the Phenomenological SLAB Wind Analysis in Section 3.2

Orbit	Seg.	MJD	Precession Phase	Clean Exposure (s)	Hp Count Rate (s^{-1})	Mp Count Rate (s^{-1})
1	S1	60563.549 ± 0.053	0.00270 ± 0.00156	6475	12.98	1.35
	S2	60563.686 ± 0.050	0.00673 ± 0.00148	5724	14.53	1.66
	S3	60563.804 ± 0.043	0.01022 ± 0.00126	5108	14.81	1.83
	S4	60563.891 ± 0.043	0.01275 ± 0.00128	5209	15.25	1.86
	S5	60564.113 ± 0.087	0.01928 ± 0.00257	5922	14.92	1.81
	S6	60564.281 ± 0.054	0.02421 ± 0.00158	6899	15.23	1.85
	S7	60564.414 ± 0.054	0.02812 ± 0.00158	6611	15.22	1.88
2	S8	60564.978 ± 0.088	0.04470 ± 0.00258	10,325	16.61	2.28
	S9	60565.245 ± 0.153	0.05253 ± 0.00451	17,010	17.51	2.57
	S10	60565.577 ± 0.153	0.06229 ± 0.00451	16,176	17.28	2.53
	S11	60565.941 ± 0.185	0.07299 ± 0.00544	16,981	17.46	2.55
3	S12	60566.690 ± 0.104	0.09498 ± 0.00307	10,712	17.31	2.49
	S13	60566.972 ± 0.152	0.10326 ± 0.00447	16,974	17.73	2.62
	S14	60567.301 ± 0.148	0.11294 ± 0.00435	16,142	17.86	2.66

Note. The values of MJD and precession phase refer to the centroids of the relevant segments. The uncertainties on the MJD and precession phase indicate the segment duration rather than statistical uncertainties.

Table 5
Details of Time-resolved XRISM Analysis, where All High-flux Periods of Time Were Split Into 10 Segments, Used in the Physical PION Wind Analysis in Section 3.3

Orbit	Seg.	MJD	Precession Phase	Clean Exposure (s)	Hp Count Rate (s^{-1})	Mp Count Rate (s^{-1})
1	P1	60563.580 ± 0.090	0.00363 ± 0.00264	9393	13.39	1.44
	P2	60563.785 ± 0.084	0.00966 ± 0.00247	9776	14.87	1.80
	P3	60564.015 ± 0.120	0.01641 ± 0.00354	6804	14.92	1.79
	P4	60564.252 ± 0.083	0.02336 ± 0.00243	9413	15.26	1.88
	P5	60564.413 ± 0.054	0.02811 ± 0.00157	6611	15.22	1.88
2	P6	60564.978 ± 0.088	0.04470 ± 0.00258	10,325	16.61	2.28
	P7	60565.311 ± 0.220	0.05449 ± 0.00646	23,864	17.48	2.57
	P8	60565.843 ± 0.284	0.07010 ± 0.00833	26,303	17.37	2.54
3	P9	60566.690 ± 0.104	0.09498 ± 0.00307	10,712	17.31	2.49
	P10	60567.134 ± 0.315	0.10804 ± 0.00925	33,147	17.79	2.64

Note. The values of MJD and precession phase refer to the centroids of the relevant segments. The uncertainties on the MJD and precession phase indicate the segment duration rather than statistical uncertainties.

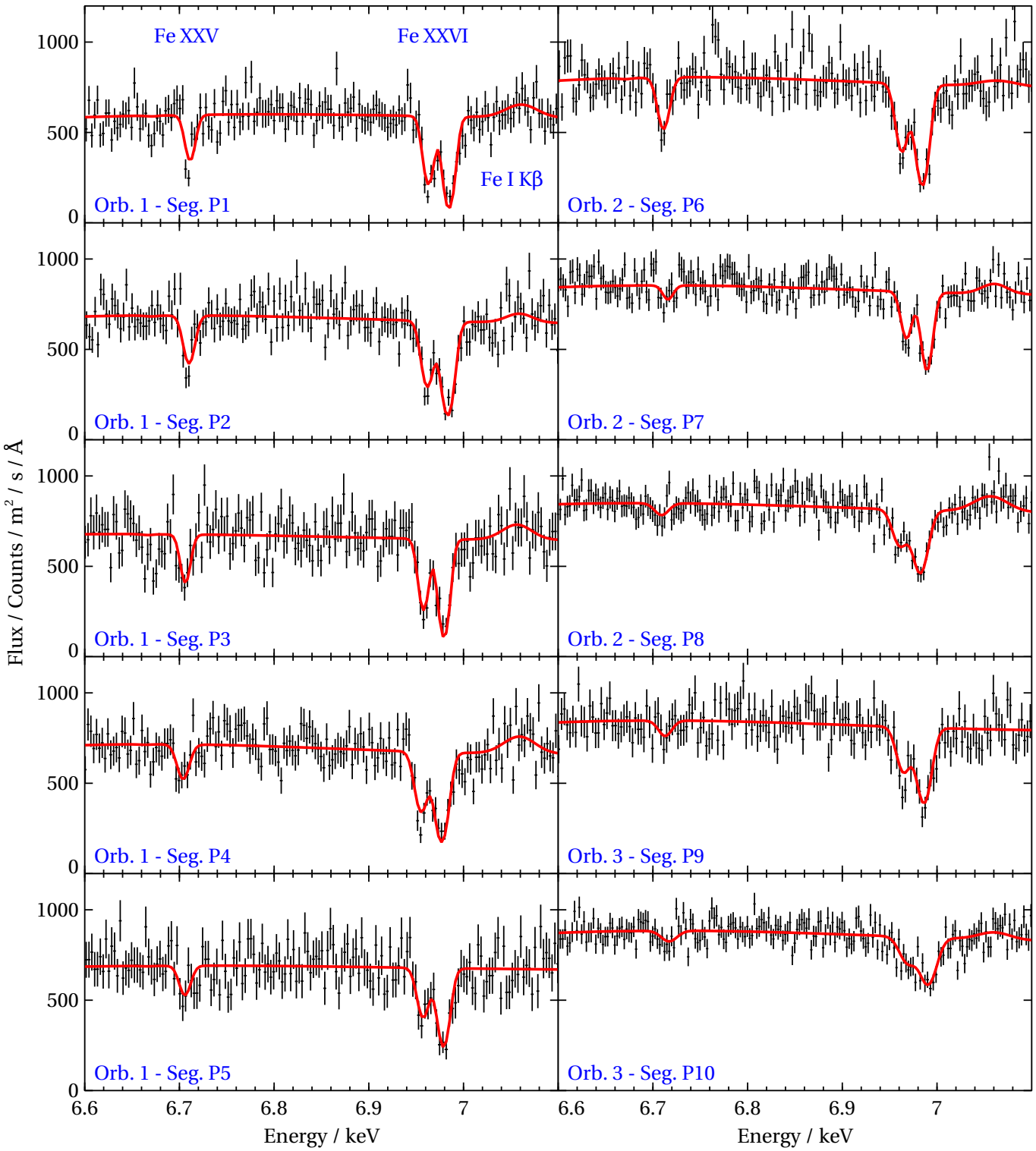

Figure 8. Narrow-band XRISM spectra focusing on the Fe XXV and XXVI energy region from the physical time-resolved analysis (using the PION model) split into 10 segments alongside the best-fitting spectral model. Only Hp event spectra are shown. The top left panel includes labels describing the different spectral features observed in Her X-1. We use the segment numbering scheme (from P1 to P10) defined in Table 2. The X and Y axes ranges are the same for all panels.

Appendix B
Elemental Abundance Analysis

We leverage the simultaneous XRISM, XMM-Newton, and NuSTAR data to perform the most detailed elemental abundance analysis of the disk wind of Her X-1 to date. We previously analyzed the wind abundances in P. Kosec et al. (2023a) and P. Kosec et al. (2023b) using XMM-Newton and Chandra data separately. However, the spectral resolution of XRISM in the Fe K band allows us to perform a much more robust analysis by resolving the complex structure in this energy band and accurately measuring the wind ionization parameter. XMM-Newton RGS data inform us about the abundances of lighter elements such as C, N, O, Ne, and Mg with transitions in the

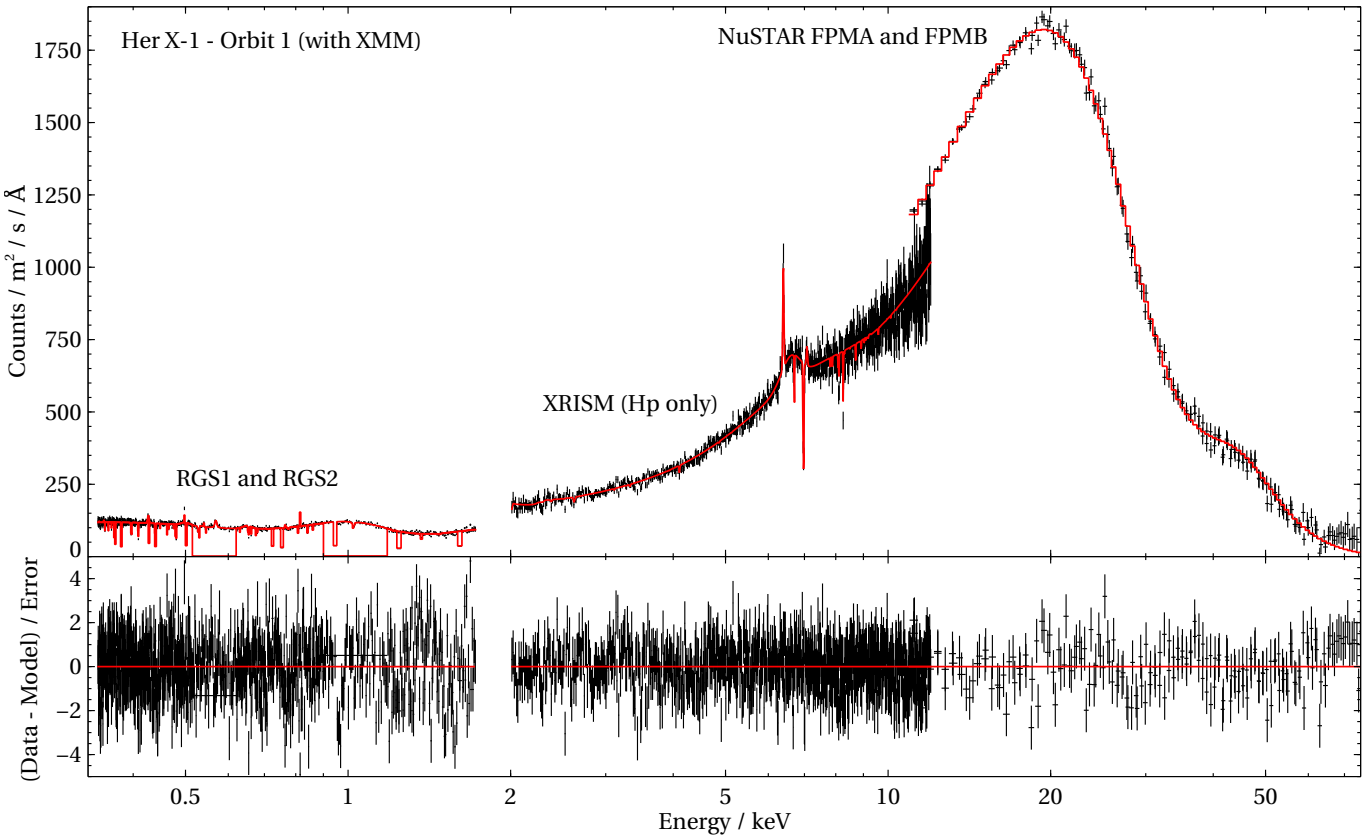

Figure 9. The full-band spectral fit of Orbit 1 (with XMM) using the final PION model with the best-fitting disk wind elemental abundances, alongside the residuals to this fit (lower panel). XMM-Newton RGS 1, 2, XRISM (Hp events only), NuSTAR FPMA, and FPMB data are shown. We note that most of the spikes across the RGS 1 and 2 models are not imprinted by the disk wind but are due to instrumental features (CCD chip gaps).

0.35−1.75 keV band. On the other hand, the energy band of XRISM (1.8−12 keV) contains transitions of heavier elements including Si, S, Ar, Ca, Fe, and Ni. Therefore, to extract the maximum amount of information, we combine both datasets. Since the disk wind is highly ionized and its signatures are the metallic lines of these elements (with no H lines within this X-ray range), we cannot extract the elemental abundances with respect to the abundance of hydrogen. Instead, we must compare the abundance with respect to one reference metal. Following our previous work (P. Kosec et al. 2023a), we primarily choose O to be the reference and fix its abundance to 1. This choice is used in the PION spectral analysis in Section 3.3. For completeness, we also list the best-fitting abundance values assuming Fe as the reference element. This choice allows a direct comparison with the abundance study of disk winds in four low-mass X-ray binaries by N. Keshet et al. (2025).

To leverage as much information as possible, we use all data from the 2024 campaign on Her X-1. However, as the disk wind is strongly variable, the data must be split and care must be taken in any simultaneous fitting. The XMM-Newton observations occurred during XRISM Orbits 1 and 3 but covered only parts of those orbits (compared with XRISM, which covered full orbits). For this reason, we split the XRISM data from those orbits into two spectral data groups—one spectrum simultaneous with the XMM-Newton pointing, and one spectrum nonsimultaneous with XMM-Newton. There was no XMM-Newton observation during Orbit 2, and so those XRISM data form their own data group. We also add the NuSTAR observations in each data group for accurate SED modeling (required by the PION wind model)—the NuSTAR observation which occurred during Orbit 2 for all data taken during Orbits 1 and 2, and the NuSTAR observation taken during Orbit 3 for all data from Orbit 3. Then we fit all these five data groups simultaneously, without any stacking—Orbit 1 (no XMM), Orbit 1 (with XMM), Orbit 2 (no XMM), Orbit 3 (XMM), and Orbit 3 (no XMM). Cross-calibration constants are used to account for calibration differences between the different instruments, as well as to account for variability in the hard energy band covered by the NuSTAR data.

The spectral model used is similar to the one in Section 3.2, but the phenomenological SLAB absorber model is replaced with a PION component. Moreover, we add several extra spectral components to describe the RGS data and accurately describe the entire SED of Her X-1 from 0.35 to 75 keV. These spectral components are taken from P. Kosec et al. (2022). The RGS spectrum is described with a combination of a regular BB (0.05 keV temperature, likely from direct disk emission), a blackbody modified with coherent Compton scattering (reprocessing of primary accretion column radiation with a temperature of 0.1−0.2 keV), a broad Gaussian line near 1 keV (Fe L emission), two medium-width emission lines (O VIII and N VII emission) and two narrow emission lines (O VII and N VI emission). For those data groups with no XMM coverage, we link the RGS component parameters to the best-fitting values from the nearby data groups with XMM coverage. Considering the evolution of the XRISM lightcurve (Figure 1), Orbit 1 (no XMM) has its RGS component parameters fixed to those from Orbit 1 (with XMM). Orbit 2 and Orbit 3 (no XMM) data groups have the RGS component parameters fixed to those from Orbit 3 (with XMM). One of these full-band spectral fits (Orbit 1 with XMM) is shown in Figure 9.

Table 6
Best-fitting Elemental Abundances of the Disk Wind of Her X-1 from a Simultaneous Analysis of All XRISM, XMM-Newton, and NuSTAR Data from the 2024 Campaign

Element	C	N	O	Ne	Mg	Si	S	Ar	Ca	Fe	Ni
Abundances	$0.00^{+0.08}$	$2.2^{+0.8}_{-0.7}$	1 (ref.)	$1.6^{+0.4}_{-0.3}$	$0.7^{+0.5}_{-0.4}$	$0.6^{+0.3}_{-0.2}$	$0.62^{+0.17}_{-0.15}$	$0.5^{+0.3}_{-0.3}$	$1.4^{+0.4}_{-0.3}$	$0.70^{+0.08}_{-0.10}$	$1.3^{+0.3}_{-0.3}$
	$0.0^{+0.1}$	$3.2^{+1.0}_{-1.0}$	$1.45^{+0.19}_{-0.17}$	$2.2^{+0.5}_{-0.4}$	$1.0^{+0.7}_{-0.5}$	$0.8^{+0.4}_{-0.3}$	$0.9^{+0.2}_{-0.2}$	$0.7^{+0.5}_{-0.5}$	$2.0^{+0.5}_{-0.5}$	1 (ref.)	$1.9^{+0.3}_{-0.3}$

Note. The first row shows the results of a spectral analysis assuming O as the reference element (the abundance of which is fixed to 1), while the second row shows the results of a spectral analysis assuming Fe as the reference element.

All of the other spectral fit parameters are left free to vary (and are decoupled between the five data groups) except the elemental abundances in the PION component, which are all coupled among the five data groups. We note that all relevant elemental abundances across the XMM-Newton and XRISM energy bands are fitted (except the reference elements O or Fe) regardless of the signal-to-noise ratio, as leaving them fixed to 1 may bias the spectral fit. This very complex spectral model is then fitted in SPEX and we extract its statistical uncertainties. The best-fitting elemental abundances are given in Table 6 for both the O and Fe reference spectral fits. We note that the spectral fit quality of both approaches is nearly the same, and they differ by ΔC-stat of $\sim$0.1 for 44767 degrees of freedom. However, as expected, the best-fitting wind column densities $N_{\rm H}$ are different. Setting Fe as the reference element results in 30% lower $N_{\rm H}$ column densities in each data group, caused by increasing the strength of the lines of Fe (and other elements) by the same factor.

The abundances of N and Ne are super-Solar compared with O, in agreement with previous measurements (P. Kosec et al. 2023a). The abundance of C was not previously measured in the disk wind but was found to be sub-Solar (C/O of 0.3−0.6) in Her X-1 using Low state observations (M. A. Jimenez-Garate et al. 2002). Here we only obtained a very stringent upper limit of 0.08 on its value. The discrepancy with the study of M. A. Jimenez-Garate et al. (2002) could be introduced if there is a strong emission line component of C VI below the wind absorption, that may not necessarily be related to the disk wind. Due to low Doppler shifts of the wind, if there exists such a component, this would be very hard to separate, especially in RGS data. This same caveat in principle applies to all elemental measurements.

The abundances of Mg, Si, S, and Ar are mildly sub-Solar, but have relatively large uncertainties. They are all consistent with the abundance of Fe at 1σ uncertainties. Our previous study using Chandra HETG (P. Kosec et al. 2023b) indicated a super-Solar abundance of Mg, Si, and S; however, our current results cannot be directly compared to that study, because in P. Kosec et al. (2023b) we fixed the abundances of both O and Fe to the best-fitting values from P. Kosec et al. (2023a). On the other hand, the abundances of Ca and Ni are super-Solar, but again with significant uncertainties (abundances are consistent with Fe at 2σ level).

The biggest surprise is the abundance of Fe, which is tightly constrained to $0.70^{+0.08}_{-0.10}$. This result is in significant tension with previous XMM-Newton results which indicated an abundance of 2.1 ± 0.3. We investigated this difference using the simultaneous XMM-Newton EPIC-pn and XRISM data. To simplify the comparison as much as possible, we used the phenomenological SLAB model to fit the strength of the Fe XXV and XXVI lines. We found that EPIC-pn consistently overestimated the strength of these lines. If the Fe XXV/XXVI lines are overestimated in spectral modeling, the physical PION component will require a high $N_{\rm H}$ column density or a high Fe abundance. This overestimation is likely due to the limited spectral resolution of EPIC-pn in the Fe K energy band, the degeneracy between the optical depth of the wind absorption lines (at 6.7 and 7.0 keV), and the strength of the broadened Fe XXV emission line at the same location at 6.7 keV. Fixing the Fe abundance in the EPIC-pn data in a wind model using PION to the value from the current combined analysis (Fe = 0.7) instead resulted in much higher column densities, underlying this disk wind-emission line degeneracy.

The spectral resolution of XRISM allowed us to finally resolve the individual features of the complex Fe K band of Her X-1, resulting in a much more confident measurement of the Fe line optical depths, and so a more confident measurement of the Fe/O elemental abundance ratio. It could be possible to further improve the quality of this elemental abundance study to include all of the previous high-quality XMM-Newton (primarily RGS) data from the 2020 campaign as well as the Chandra HETG data. This would primarily reduce the uncertainties on the lighter elements within the RGS energy band (considering the wealth of available XMM-Newton data) such as C, N, O, Ne, and Mg. This is beyond the scope of the current paper as it would require more significant computational resources and is left for a future study.

ORCID iDs

Peter Kosec https://orcid.org/0000-0003-4511-8427
Laura Brenneman https://orcid.org/0000-0003-2663-1954
Erin Kara https://orcid.org/0000-0003-0172-0854
Teruaki Enoto https://orcid.org/0000-0003-1244-3100
Takuto Narita https://orcid.org/0009-0006-7889-6144
Koh Sakamoto https://orcid.org/0009-0007-8032-3641
Rüdiger Staubert https://orcid.org/0000-0003-1498-1543
Francesco Barra https://orcid.org/0000-0001-5852-6740
Andrew Fabian https://orcid.org/0000-0002-9378-4072
Jon M. Miller https://orcid.org/0000-0003-2869-7682
Ciro Pinto https://orcid.org/0000-0003-2532-7379
Daniele Rogantini https://orcid.org/0000-0002-5359-9497
Dominic Walton https://orcid.org/0000-0001-5819-3552
Yutaro Nagai https://orcid.org/0009-0003-9261-2740

References

Arnaud, K. A. 1996, ASPC, 101, 17
Begelman, M. C., McKee, C. F., & Shields, G. A. 1983, ApJ, 271, 70
Boroson, B., Kallman, T., & Vrtilek, S. D. 2001, ApJ, 562, 925
Cash, W. 1979, ApJ, 228, 939
Castro Segura, N., Knigge, C., Long, K. S., et al. 2022, Natur, 603, 52
Deeter, J. E., Boynton, P. E., & Pravdo, S. H. 1981, ApJ, 247, 1003
den Herder, J. W., Brinkman, A. C., Kahn, S. M., et al. 2001, A&A, 365, L7

de Plaa, J., Kaastra, J. S., Tamura, T., et al. 2004, A&A, 423, 49
Díaz Trigo, M., Sidoli, L., Boirin, L., & Parmar, A. N. 2012, A&A, 543, A50
Gallegos-Garcia, M., Jacquemin-Ide, J., & Kalogera, V. 2024, ApJ, 973, 168
Gerend, D., & Boynton, P. E. 1976, ApJ, 209, 562
Harrison, F. A., Craig, W. W., Christensen, F. E., et al. 2013, ApJ, 770, 103
HI4PI Collaboration, Ben Bekhti, N., Flöer, L., et al. 2016, A&A, 594, A116
Hölzer, G., Fritsch, M., Deutsch, M., Härtwig, J., & Förster, E. 1997, PhRvA, 56, 4554
Ishisaki, Y., Kelley, R. L., Awaki, H., et al. 2022, SPIE, 12181, 121811S
Jansen, F., Lumb, D., Altieri, B., et al. 2001, A&A, 365, L1
Jimenez-Garate, M. A., Hailey, C. J., den Herder, J. W., Zane, S., & Ramsay, G. 2002, ApJ, 578, 391
Jimenez-Garate, M. A., Raymond, J. C., Liedahl, D. A., & Hailey, C. J. 2005, ApJ, 625, 931
Kaastra, J. S., & Bleeker, J. A. M. 2016, A&A, 587, A151
Kaastra, J. S., Mewe, R., & Nieuwenhuijzen, H. 1996, in 11th Colloq. on UV and X-ray Spectroscopy of Astrophysical and Laboratory Plasmas (Univ. Academy Press), 411
Kaastra, J. S., Steenbrugge, K. C., Raassen, A. J. J., et al. 2002, A&A, 386, 427
Katz, J. I. 1973, NPhS, 246, 87
Keshet, N., Behar, E., & Miller, J. M. 2025, ApJ, 990, 186
Kosec, P., Fabian, A. C., Pinto, C., et al. 2020, MNRAS, 491, 3730
Kosec, P., Kara, E., Fabian, A., et al. 2023a, NatAs, 7, 715
Kosec, P., Kara, E., Fabian, A. C., et al. 2022, ApJ, 936, 185
Kosec, P., Kara, E., Fabian, A. C., et al. 2023b, ApJ, 959, 51
Kosec, P., Pinto, C., Walton, D. J., et al. 2018, MNRAS, 479, 3978
Kosec, P., Rogantini, D., Kara, E., et al. 2024, ApJ, 972, 32
Kotani, T., Ebisawa, K., Dotani, T., et al. 2000, ApJ, 539, 413
Leahy, D. A., & Abdallah, M. H. 2014, ApJ, 793, 79
Lee, J. C., Reynolds, C. S., Remillard, R., et al. 2002, ApJ, 567, 1102
Mehdipour, M., Kaastra, J. S., & Kallman, T. 2016, A&A, 596, A65
Miura, D., Yamaguchi, H., Ballhausen, R., et al. 2025, PASJ, 77, psaf057
Mochizuki, Y., Tsujimoto, M., Kelley, R. L., et al. 2024, ApJL, 977, L21
Muñoz-Darias, T., Jiménez-Ibarra, F., Panizo-Espinar, G., et al. 2019, ApJL, 879, L4
Neilsen, J., & Degenaar, N. 2023, in High-Resolution X-ray Spectroscopy: Instrumentation, Data Analysis, and Science, ed. Cosimo Bambi (Springer), 291
Parra, M., Petrucci, P. O., Bianchi, S., et al. 2024, A&A, 681, A49
Pinto, C., Middleton, M. J., & Fabian, A. C. 2016, Natur, 533, 64
Ponti, G., Fender, R. P., Begelman, M. C., et al. 2012, MNRAS, 422, L11
Reynolds, A. P., Quaintrell, H., Still, M. D., et al. 1997, MNRAS, 288, 43
Sánchez-Sierras, J., & Muñoz-Darias, T. 2020, A&A, 640, L3
Scott, D. M., Leahy, D. A., & Wilson, R. B. 2000, ApJ, 539, 392
Staubert, R., Klochkov, D., Vybornov, V., Wilms, J., & Harrison, F. A. 2016, A&A, 590, A91
Strüder, L., Briel, U., Dennerl, K., et al. 2001, A&A, 365, L18
Tananbaum, H., Gursky, H., Kellogg, E. M., et al. 1972, ApJL, 174, L143
Tashiro, M. S. 2022, IJMPD, 31, 2230001
Tetarenko, B. E., Lasota, J. P., Heinke, C. O., Dubus, G., & Sivakoff, G. R. 2018, Natur, 554, 69
Tombesi, F., Cappi, M., Reeves, J. N., et al. 2010, A&A, 521, A57
Truemper, J., Pietsch, W., Reppin, C., et al. 1978, ApJL, 219, L105
Ueda, Y., Inoue, H., Tanaka, Y., et al. 1998, ApJ, 492, 782
Ueda, Y., Murakami, H., Yamaoka, K., Dotani, T., & Ebisawa, K. 2004, ApJ, 609, 325
Weisskopf, M. C., Tananbaum, H. D., Van Speybroeck, L. P., & O'Dell, S. L. 2000, SPIE, 4012, 2
XRISM Collaboration, Audard, M., Awaki, H., et al. 2024, ApJL, 977, L34